TÉCNICO LISBOA

Super Resolution Imaging of Protein Aggregates in Cell Models

Tiago Coutinho Mimoso

Thesis to obtain the Master of Science Degree in

Bioengineering and Nanossystems

Supervisors:

Prof Dr. Tiago Fleming Outeiro

Prof. Dr. João Miguel Raposo Sanches

Examination Committee

Chairperson: Prof. Jorge Manuel Ferreira Morgado

Supervisor: Prof. Dr. Tiago Fleming Outeiro

Members of the Committee: Prof. José Miguel Rino Henriques

May 2022

Declaration

I declare that this document is an original work of my own authorship. The present document fills all the requirements of the Code of Conduct and Good Practices of the Universidade de Lisboa.

Preface

The work presented in this thesis was performed at Department of Experimental Neurodegeneration at University Medizin Göttingen in Göttingen, Germany with confocal microscopy images taken at European Neuroscience Institute Göttingen in Göttingen, Germany. The work was done from March to December 2021, under the supervision of Prof. Dr. Tiago Fleming Outeiro and co-supervised at Instituto Superior Técnico by Prof. Dr. João Miguel Sanches.

Acknowledgments

First, I would like to thank to my supervisors, Prof. Dr. Tiago Fleming Outeiro and Prof. Dr. João Miguel Sanches for the guidance and support in this project between the world of biology and engineering. It was a pleasure to work with both and feel the passion in the work developed in both fields of study

A special thanks to Liana Shvachiy for teach me simple things like cell culture or simple transfection which in the beginning it was challenging in several ways. Thanks for the mentoring in all aspects of my master thesis were your dedication and knowledge were very important.

A word to friends since the high school, from the degree of Materials Engineering to the master's degree in Bioengineering and Nanossystems crossing several others where the support was amazing during these last years.

Finally, I would like to thank to my family, especially to my parents and sister that were there all the time during this small path, but I know that they will be there always.

1. Index

2. Abstract

Parkinson Disease is one of the most common neurodegenerative diseases in the world. The aggregation of proteins is one possible cause for that which needs to be studied in several aspects such as location and the interactions with the surroundings. The use of confocal and more recent Stimulated emission depletion (STED) microscopy has been one way to understand those mechanisms behind the aggregation.

HEK-293T and H4 cells were used to mimic the responses and mechanisms involved. Several protein aggregation models were employed to create a detailed analysis method to use in the images taken from the confocal, STED and expansion microscopy. The method was developed to surpass the lack of the 3rd axis in the analysis, getting the volume of the aggregates and the spatial location of them.

Our findings reveal a simple method to have the volume of protein aggregation in the models (Synphilin-1(Sph1) protein tagged with EGFP, fluorescent fragment of GFP - Sph1-GFP aggregation model - and α-Synuclein (αSyn) protein with EGFP truncated with just 83 amino acids) and Sph1 protein tagged with V5 - SynTWT+Sph1 aggregation model-). The findings reveal that there are some differences regarding the microscopy technique used in terms of volume and the number of aggregates per cell. In the SynTWT+Sph1 aggregation model, the colocalization between the proteins seems to be out of phase on the Z axis.

Keywords: α-Synuclein, Synphilin-1, Super-Resolution Microscopy, Segmentation, Deep Learning, Volume

3. Resumo

A doença de Parkinson é uma das mais comuns doenças neurodegenerativas no mundo. A agregação de proteínas é uma das possíveis causas que por essa razão leva o mesmo a ser estudado em diversos aspetos como a localização e interação com o meio que o rodeia. Usa-se a microscopia confocal e STED para que seja possível o estudo dos mecanismos que levam à doença.

Neste trabalho, usámos células HEK-293T e H4 para reproduzir a resposta e os mecanismos envolvidos. Diversos agregados proteicos foram estudados para a criação de um detalhado método para uso nas diversas técnicas de microscopia. O método foi desenvolvido com vista a suplantar a falta do terceiro eixo, podendo assim obter o volume do agregado e a sua localização.

Os resultados da análise revelam um método simples para a obtenção do volume de agregados proteicos nos modelos estudados (proteína Sinfilina-1(Sph1) marcada com EGFP, fragmento fluorescente de GFP – modelo de agregação Sph1GFP - a α-sinucleína (αSyn com EPGFP fragmentado com apenas 83 aminoácidos) e proteína Sph1 marcada com o marcador V5 – modelo de agregação SynTWT+Sph1-). Existem ainda diferenças a serem notadas relativamente ao tipo de microscopia usado nomeadamente no volume dos agregados e número de agregados por célula. No modelo de agregação SynTWT+Sph1 parece demonstrar a colocalização entre as proteínas está desfasada no eixo Z.

Palavras-chave: α-sinucleína, Sinfilina-1, Microscopia de Super-Resolução, Segmentação, Aprendizagem Profunda, Volume

4. List of figures

5. List of Abbreviations

µg ..... *micrograms*

µL ..... *microliters*

ExM ..... *Expansion Microscopy*

FWHM ..... *Full width at half maximum*

LB… ..... *Lewy Body*

ml ..... *mililiter*

NA..... *Numerical aperture*

PD ..... *Parkinson's disease*

protofibrils ..... *pre-fibrillar intermediates*

PSF..... *Point Spread Function*

PTM ..... *posttranslational modifications*

RT. ..... *Room Temperature*

SNCA..... *gene encoding α-Synuclein*

Sph1 ..... *Synphilin-1*

Sph1-GFP aggregation model..... *Sph1 protein tagged with EGFP, fluorescent fragment of GFP*

STED ..... *Stimulated emission depletion microscopy*

SynTWT+Sph1 aggregation model *(αSyn with EPGFP truncated with just 83 amino acids) and Sph1 protein tagged with V5*

αSyn ..... *α-Synuclein*

MIP ..... *Maximum Intensity Projection*

6. List of Tables

7. Introduction

Parkinson's disease

Parkinson's disease (PD) affects around 1%-1.5% of the total population (Vidyadhara et al., 2019). With the increase of the average age among the population, these age-dependent disorders are becoming a threat to human health (Gitler et al., 2017) and could achieve astonishing numbers by 2050. Parkinson's disease was named by Jean-Martin Charcot after James Parkinson describe the features of six patients. This characterization is still in use up to date for diagnosis of PD. James Parkinson published his observations in 1817 in 'An essay on the shaking palsy'(Parkinson, 2002). Then, Jean Charcot extends the initial description. Using these initial descriptions, the first hypothesis was relating the PD with epigenetics and environmental factors.

Figure 1. **Predicted structure of α-Syn in physiological conditions.** Adapted from (Lücking & Brice, 2000)

The main protein linked to PD is αSyn (Goedert, 2001). The correlation between αSyn aggregation and conformational changes and PD have been studied for the past 20 years, describing this protein as having the central role in the development and progression of the disease (Goedert, 2001; Marvian et al., 2019). After gene sequencing of PD patients, some mutations in the gene encoding α-Synuclein (*SNCA*) have been found and some of those mutations were linked to the dominantly inherited forms of PD, the familiar form of PD, which only represents 5% (Bossy-Wetzel et al., 2004; Polymeropoulos et al., 1997). The dogma that is still being discovered is how sporadic PD occurs, which represents around 95% of the disease cases (Valente et al., 2012)(Figure 1).

The symptoms of the disease are tremor, rigidity in the first steps of the disease (Huang et al., 2004; Lücking & Brice, 2000). These effects can be caused by environmental factors or genetic factors. Although many others can be associated, for example, depression or panic attacks.

Therefore, the development of PD involves several factors. Studies suggest that polymorphisms in the genes that are responsible for dopamine metabolism and transport, iron homeostasis, inflammation, mitochondrial dysfunction and exogenous or endogenous toxin metabolism might play a role in individual predisposition to developing PD (Figure 2) (Huang et al., 2004). Affecting the presynaptic αSyn, these protein create micro aggregation which theme impaired neurotransmitter release leading to postsynaptic degeneration (Schulz-Schaeffer, 2015). Also, in its aggregation, it is created LB which is a way to classify PD.

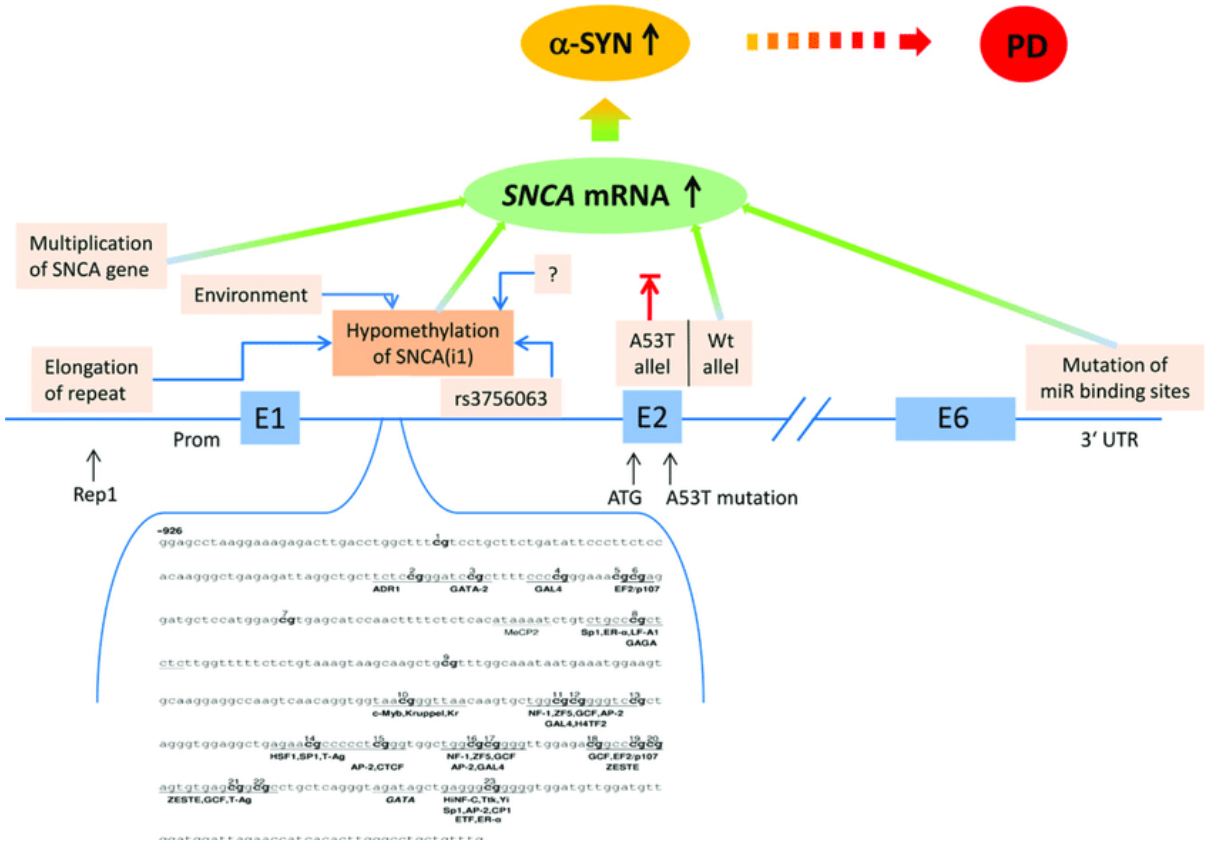

Figure 2. **αSyn- encoding genes and their relationship with several factors.** It is known that SNCA gene encodes the αSyn protein and then the evolution to possible PD stage. Adapted from (Schulz-Schaeffer, 2015)

Aggregation Models

Aggregation of αSyn is considered one of the crucial steps in PD and it is thought to precede via a seeding-nucleation mechanism. In vitro studies have revealed that αSyn aggregation is a nucleation-dependent process that initiates with the progression of monomers to oligomers to fibrils (Danzer & Mclean, 2011). Recent studies support the hypothesis that pre-fibrillar intermediates (protofibrils) and not mature amyloid fibrils, may be the key toxic species in PD (Hartl & Hayer-Hartl, 2009; Taylor et al., 2002).

α-Synuclein

As explained above, αSyn has a major role in the development of PD but also has other roles in the system. αSyn is present in dopamine neurons, the neurons affected in PD, and its aggregation (Bousset et al., 2013) in Lewy bodies (LB) is a pathological hallmark in PD. (Figure 3).

In the past years, the αSyn and the understanding about genetics has evolved tremendously and other mutations in the SNCA gene have been linked to familial forms of the disease (Appel-Cresswell et al., 2013; Chartier-Harlin et al., 2004; Fares et al., 2014; Krüger et al., 1998; Lesage et al., 2013; Pasanen et al., 2014; Polymeropoulos et al., 1997; Proukakis et al., 2013; Singleton et al., 2003; Zarranz et al., 2004). Due to the number of mutations and the role of this protein in the PD, the study of this protein increases and more recently, polymorphisms in the SNCA gene have been identified as risk factors for PD, in genome wide association studies (Blauwendraat et al., 2019; Genet, 2014).

αSyn took a centre stage in the research in recent years and now presents a central role to achieve the knowledge of the disease (Outeiro & Mestre, 2019). *In vitro* studies using recombinant αSyn were instrumental to inform about the aggregation process that culminates with the formation of typical amyloid fibrils (Conway et al., 2000; Li et al., 2001). *In vivo* studies in human αSyn transgenic and in knockout mice provided insight into both its physiological function and into the mechanisms of toxicity (Abeliovich et al., 2000; Burré et al., 2010; Greten-Harrison et al., 2010). *In vitro* studies, using mammalian and yeast cell models, yielded important insight into the molecular underpinnings of αSyn aggregation, cytotoxicity, and physiological effects (Lázaro et al., 2014; McLean et al., 2000), and into the pathways involved in the production and clearance of the protein in the cell (Cuervo et al., 2004). The explosion in the field of proteostasis in the 2000s, brought about an important knowledge on how cells and organisms handle αSyn, attempting to refold or recycle the protein into its basic components (Cuervo et al., 2004).

More recently, technological developments in biochemical, biophysical, proteomic, and imaging approaches, provided insight into the structure, chemical modifications (posttranslational modifications, PTMs), and subcellular distribution of αSyn (Gonçalves & Outeiro, 2013).

αSyn is a presynaptic protein enriched in the brain (Koprich et al., 2017; Maroteaux & Scheller, 1991). The pathways of the protein aggregation are shown in Figure 3.

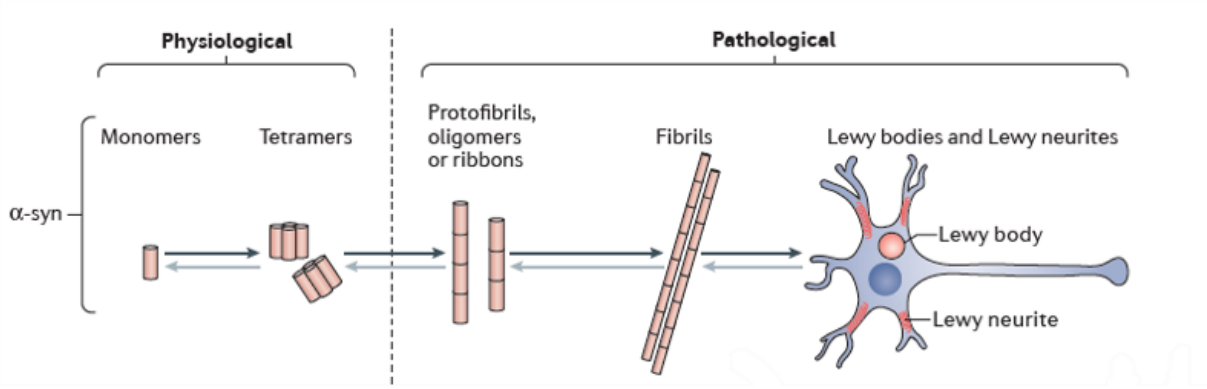

Figure 3. **αSyn pathway and its aggregation into the pathological way**. Adapted from (Koprich et al., 2017).

Synphilin-1

The formation of aggregation found in Parkinson's disease is not only composed of αSyn, some of them also composed by Sph1 (Figure 4) (Shirakashi et al., 2006). Sph1 is also a presynaptic with synaptic vesicles (Ribeiro et al., 2002) also present in LBs as well as αSyn, especially in the core region (Wakabayashi et al., 2001). Co-expression of αSyn and Sph1 in cellular models gives rise to eosinophilic cytoplasmic inclusions, and the overexpression of Sph1 alone can also produce inclusions in cultured cells. Additionally, Sph1 overexpression increases the vulnerability to the toxicity of proteasome inhibitors (Tanaka et al., 2004).

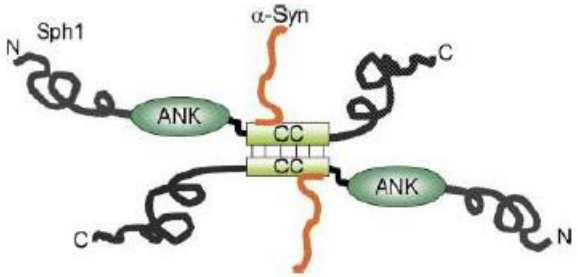

Figure 4. **Site of interaction between αSyn and synphilin-1. Schematic representation of the interaction between synphilin-1 and αSyn**. Adapted from (Xie et al., n.d.)

Sph1 is composed of 919 amino acid residues and co-localizes with αSyn in LB, in brains of PD patients (Engelender et al., 1999). Association of Sph1 with αSyn has been described as essential for targeting LB-like protein aggregates in cell culture. Given the presynaptic location and its affinity for membranes and lipids (Swinnen et al., 2011) (more specifically, binding to lipid rafts), Sph1 also seems to be required for inclusion formation (Büttner et al., 2010) and might act as an adaptor protein, anchoring αSyn to other proteins (like proteins involved in vesicular transport or cytoskeletal function) (Lücking & Brice, 2000). The interaction between the αSyn and Sph1 occurs through the C-terminus of αSyn

which is closely associated with the C-terminus of Sph1. A weak interaction occurs between the N-terminus of αSyn and Sph1 (Kawamata et al., 2001). Thus, showing that these proteins can also interact and interfere in the progression of PD(Bonin et al., 2008).

Recent studies show that synphilin-1 contains four ankyrin repeat domains and a coiled-coil domain in the central portion that specifically interacts/binds with αSyn, via the N-terminal residues of αSyn (Figure 4 and Figure 5) (Xie et al., 2010). This specific interaction significantly promotes formation and accumulation of cellular inclusions that are probably composed of αSyn (Xie et al., 2010).

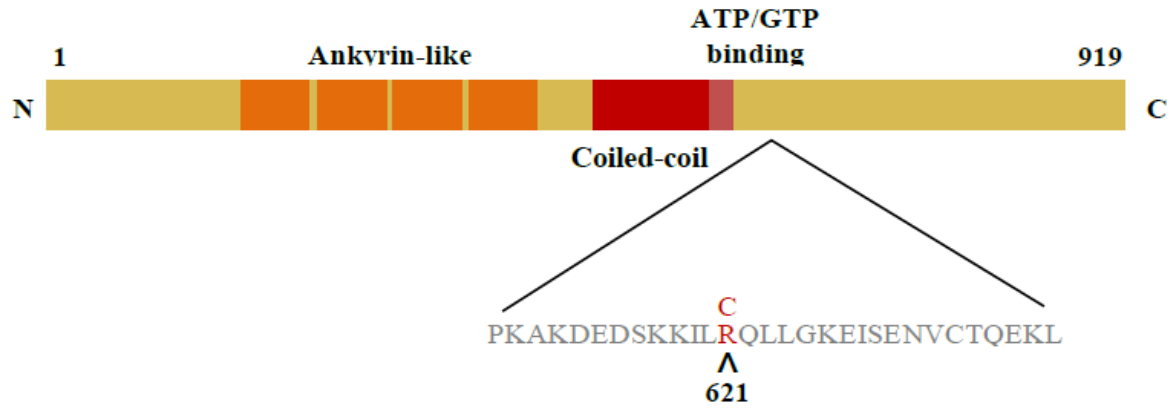

Figure 5. **Schematic representation of the synphilin-1 protein.** Different structural features are highlighted. The R621C mutation is localized in a highly conserved region. Adapted from (Bonin et al., 2008)

Cellular models of PD

In vitro studies of the aggregation involved in several neurodegenerative diseases have to be performed using cellular models to mimic the effect that this aggregation can have in the human body. Several models can be studied involving several cell lines and proteins of interest.

Given the importance of local structural effects on the aggregation of αSyn, it will be crucial to elucidate how other alterations, such as those induced by αSyn mutations, might modulate its aggregation.

The use of Sph1-GFP aggregation model takes advantage of the reliability and simplicity of the cells involved. The kidney epithelial cells(HEK-293T) is a cell line very used in some models regarding the neurodegeneration (Varghese et al., 2006). This model is composed by a Sph1 protein tagged with EGFP, fluorescent fragment of GFP (Sph1-GFP aggregation model).

The SynTWT+Sph1 aggregation model was performed in H4 cells due to being an alternative for primary neurons despite their immortal nature. Therefore, the model is composed of two independent proteins: SynT (αSyn with EPGFP truncated with just 83 amino acids) and Sph1 protein tagged with V5 The V5 tag is used majority for ELISA, flow cytometry, immunofluorescence or to western blotting (*V5 Tab Properties*, n.d.).

Microscopy

Microscopy has been one of the best sources of information in several areas like biomedical science or even materials science. Developing these techniques is mandatory to assist different areas of interest. The overcoming of the diffraction limit, the possibility of removing the out-of-focus light from the detector are some of the achievements that have been already done before, however, more challenges are existing to overcome for the field.

Confocal Microscopy

The concept of a confocal microscope was patented by Marvin Minsky in 1957. Then, M. David Egger and Paul Davidovits published two papers describing the first confocal laser scanning microscope in 1969 and 1971 respectively (Davidovits & Egger, 1971; DAVIDOVITS, 1969) at Yale University. The development of confocal microscope has been done in parallel with advances in computers, lasers, digital imaging software. Firstly, the confocal microscope showed to have biological applications in mid-1980s until became commercially available in the late 1980s. Development in design, more stable and powerful lasers, more efficient mirrors, and lower noise photodetectors have led to an improvement of confocal microscopes during the years. The ability of using this technique in several applications from cell biology to optics and crystallography shown afterwards being an important feature in confocal microscopy.(Matsumoto, 2002)

In light microscopy, illumination light is passed through the sample as uniformly as possible over the field of view. For teacher samples, where the objective lens does not have sufficient depth of focus, light from sample planes above and below the focal plane will also be detected. The out-of-focus light will add blur to the image reducing resolution (Elliott, 2020; Pawley, 2006).

In fluorescence microscopy, any dye molecules in the field of view will be stimulated, including those in out-of-focus planes. Confocal microscopy provides a means of rejecting the out-of-focus light from the detector such that it does not contribute with blur to the image that is being collected. This technique allows for high resolution imaging in thick tissues (Elliott, 2020).

One barrier achieved was the resolution limit (maximum resolution between 200-350nm) due to the wavelength of the light in the visible region as it is explained in the Abbe equation(1).

$$d = \frac{\lambda}{2 \cdot n \cdot sin\sigma} = \frac{\lambda}{2 \cdot NA}$$ (Lipson et al., 1995)

(1)

The portion of the denominator nsinθ is the numerical aperture (NA) and can reach about 1.4–1.6 in modern optics, hence the Abbe limit is d =λ/2.8 (Lipson et al., 1995).

Considering green light around 500 nm and a NA of 1, the Abbe limit is roughly d =λ/2 = 250 nm (0.25µm), which is small compared to most biological cells (1µm to 100µm), but large compared to viruses (100 nm), proteins (10 nm) and less complex molecules (1 nm). Therefore, the conventional microscopy needs to be updated or it is needed to find another way of analysing.

The confocal microscopy increases the resolution compared with conventional optical microscopy due to the fact of having the Pinhole which leads to the exclusion of the light from the non-focal plane. To explain it in a better way. In Figure *6*, using the conventional microscope the record in the focal plane will be the fluorescence of all samples instead, in the confocal microscopy, using the pinhole of the epifluorescence microscopy which is able to deny the fluorescence from the non-focal plane.

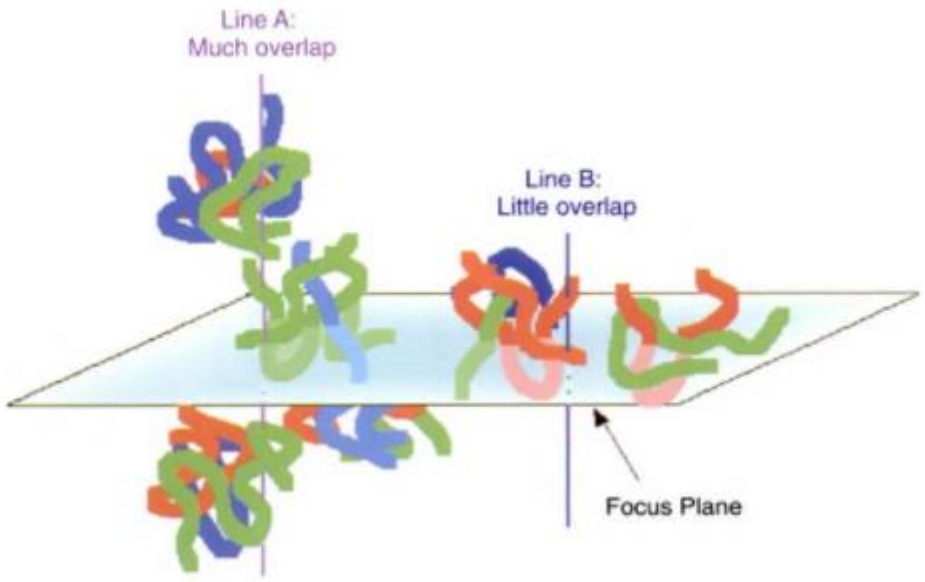

Figure 6. **View of Focal Plane. Principle of confocal microscopy and how to improve the resolution in x,y,z axis.** Adapted from (Pawley, 2006).

STED

The wavelength barrier of light microscopy led to the development of STED. STED was developed by Stefan W. Hell and Jan Wichmann in 1994 (Hell & Wichmann, 1994) resulting into a Nobel Prize in 2014. This discovery led to overcoming the diffraction limit reaching 35nm of resolution (Hell & Wichmann, 1994). STED microscopy has been used in static conditions (D'Este et al., 2015) although it hs been

shown several advantageous in other areas like live cell imaging or in vivo imaging (Wegner, Ilgen, Gregor, van Dort, et al., 2017) or materials science.

The STED microscopy is based on the confocal where it excites the sample with fluorescence particles and then a second laser bean where it is depleted of some of those fluorescence. Using this technique, the Abbe diffraction limit (Equation (1)) is overcome, and the wavelength barrier is broken. The layout of the STED microscope is present in Figure 7. In the Figure 7, it is seen that both beans are interacting. The excitation and STED beans are triggered at different times to get the better resolution. The difference between the resolution of confocal microscopy and STED is shown in Figure 7. The resolution of the STED microscope is a function of the spatial distribution and magnitude of the intensity of the depleting light, with no theoretical limit to the ultimate achievable value. Nonetheless, the nature and factual quality of the focal intensity patterns of the STED beam strongly impacts the resolution achieved by a particular configuration. Typically, a doughnut shaped distribution is targeted to obtain the most uniform resolution increase in the focal plane.

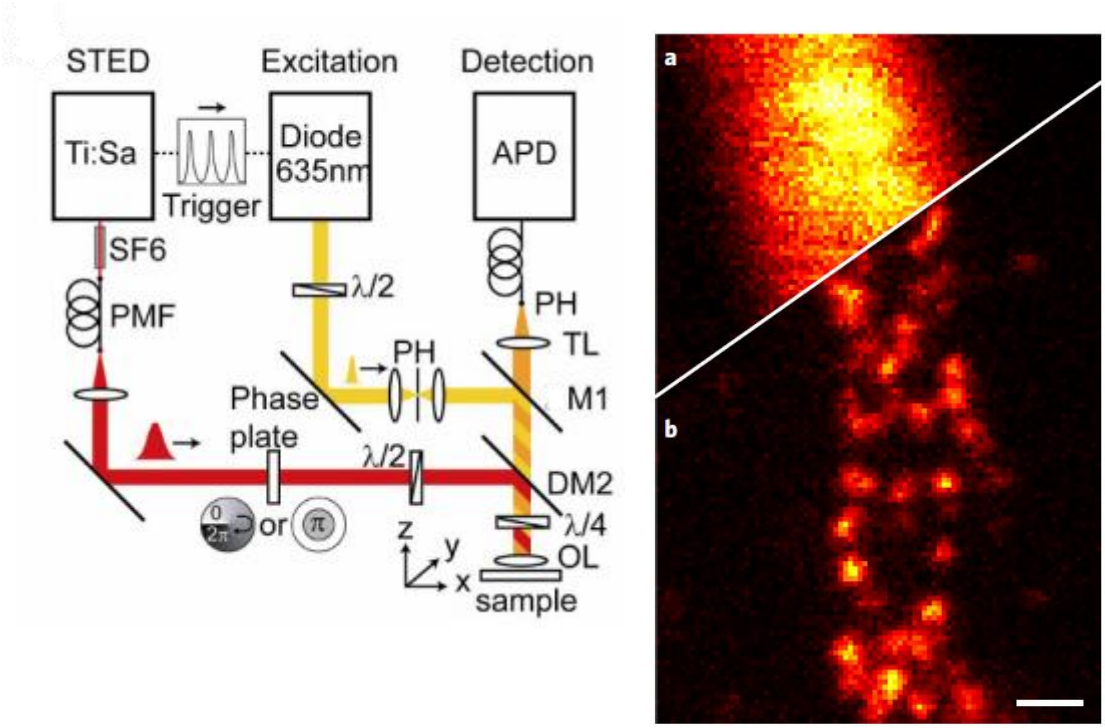

Figure 7**. Layout of STED microscope.** The layout of the STED microscope and also the number of laser beans need to have results applying this technique. Adapted from (Harke et al., 2008) (left). Confocal and STED example. Picture taken from the same sample a. confocal microscopy b. STED microscopy. Adapted from (Weber et al., 2021).

Therefore, the function the describe the doughnut shape can be described as FWHM (Full width at half maximum) function and the resulting spot has been shown to depend on the inverse square root of the saturation factor.

$$\Delta x \propto \frac{\lambda}{n\sqrt{\zeta}}$$ (Harke et al., 2008)

(2)

Where λ is the inhibition wavelength, n is the refractive index and ζ denotes the saturation factor which is defined as:

$$\zeta = \frac{I_{STED}}{I_S}$$ (Harke et al., 2008)

(3)

I_{STED} is the maximum of the intensity distribution of the inhibition light and I_s is the effective saturation intensity which can be defined as the intensity at which the probability of fluorescence emission is reduced by half.

In recent years, the development of 3D images proved to be a challenge. To overcome that issue and create the same principle of depletion in the remaining axe. Described in (van Dort, 2018) and Figure *8*, the resolution in the axial axes improves in a way of getting the real excited area as a ball instead of a cylinder.

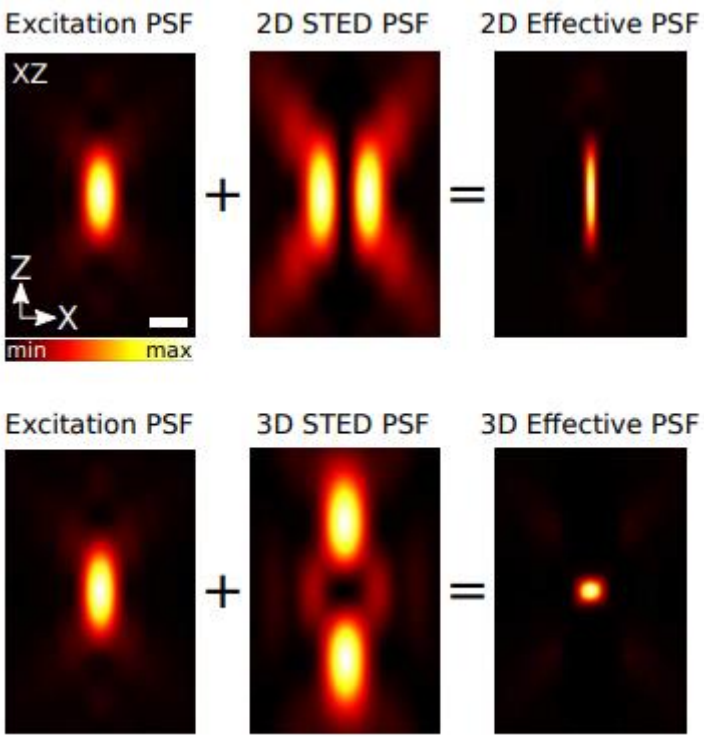

Figure 8. **Comparison between the PSF (Point Spread Function) of 2D STED or 3D STED.** The PSF give the interference of the excitation in the sample, in other words, it is the noise produced by the excitation laser. Adapted from (van Dort, 2018)

Expansion Microscopy

Expansion microscopy (ExM) is a novel super-resolution microscopy technique that was developed with the intent of creating a technique that was not bound by the necessity of very expensive microscopy. The ability of using in any setup becomes of the most advantage of this method as all the

effects are done on the sample (Truckenbrodt et al., 2018). ExM, a technique introduced by the Boyden laboratory, is an important step in the direction of becoming the biological samples that had enough resolution without special equipment.

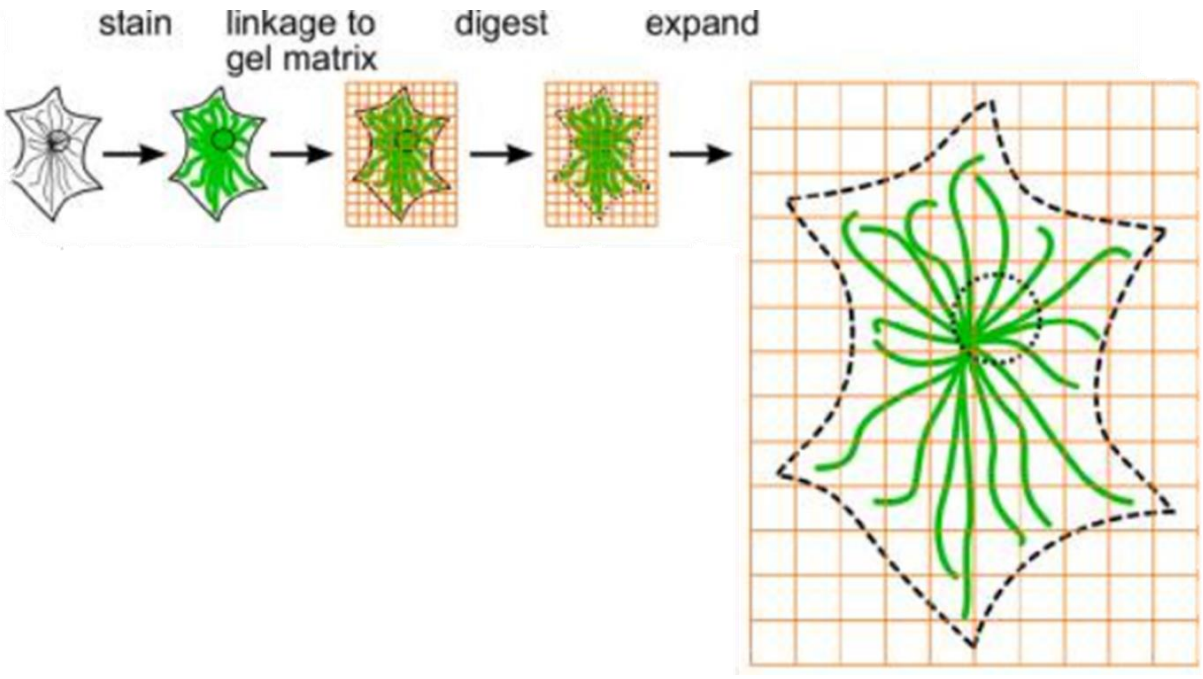

Figure 9**. Steps in the ExM protocol.** First step is the staining the protein of interest, second step is connect and linkage the biological sample with the gel matrix, third step and fourth step is digest the sample to have a homogeneous expansion, finally, the last step is expansion and imaging the gel. Adapted from (Chozinski et al., 2016)

Therefore, ExM is based on zooming out the sample to then being able to detect small distances in the sample (Chozinski et al., 2016). The normal microscopy is based on ways to zoom in into the sample and better detectors. Due to the function role of it, the only way to differentiate regions of interest is by detecting different information in various detector positions.

ExM entails that the sample of interest is first fixed, permeabilized, and immunoassays and is then embedded in polyelectrolyte gels, which expand strongly when dialyzed in water as it is shown in the Figure *9*. This technique can be used with different staining which means that we keep using the same type of staining that it has been used in the previous years

In the Figure *10*, the difference between the image taken before expansion (a) and after expansion (b). The ability to separate two fluorescence points makes it appealing to use in several applications.

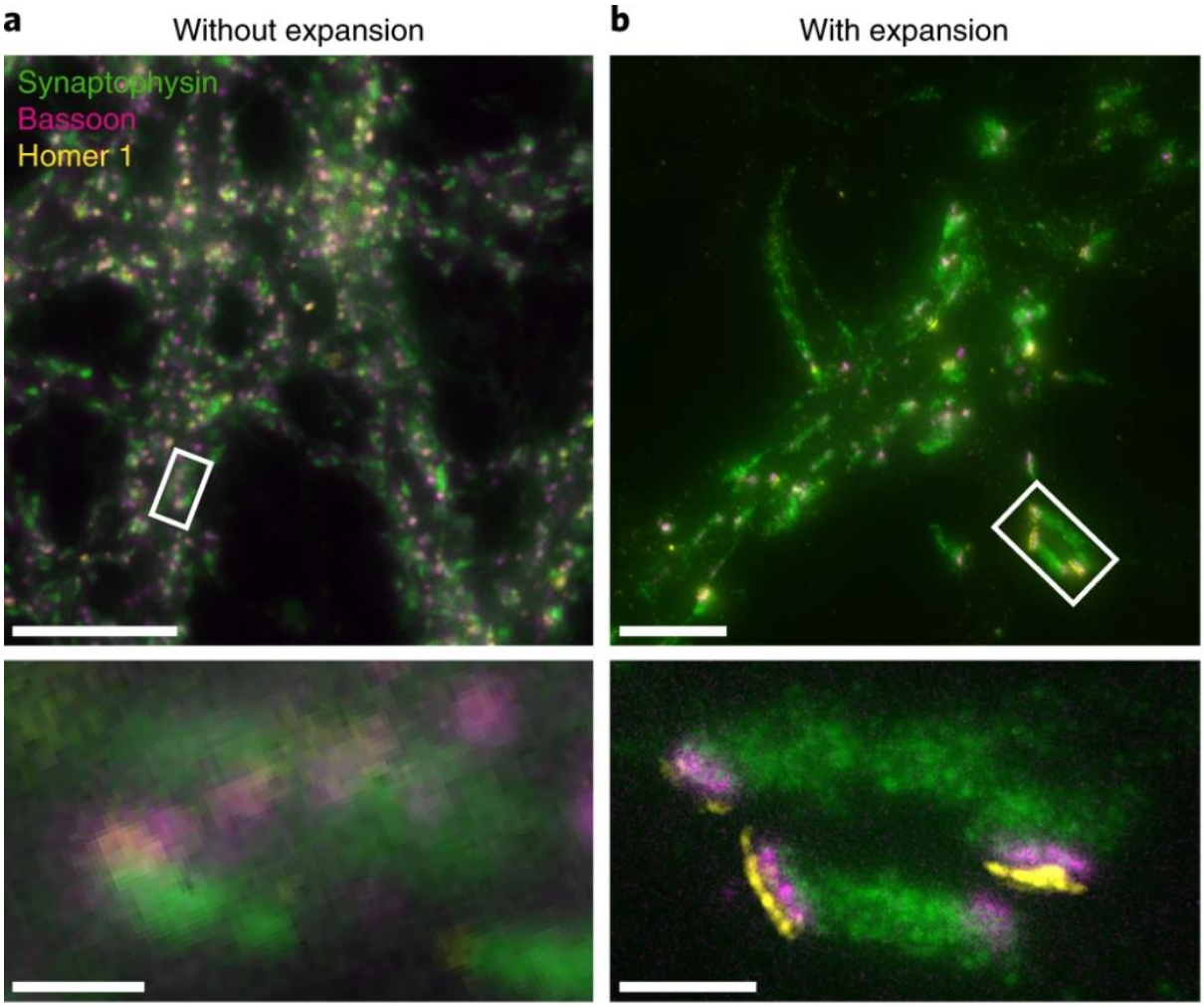

Figure 10. **Example of ExM without and with expansion.** a. Representative image (top) of neuronal cell cultures stained for synaptophysin (green), a synaptic vesicle marker; Bassoon (magenta), an active zone protein; and Homer 1 (yellow), a postsynaptic density protein. The sample was imaged on a wide-field microscope without expansion. The boxed region with individual synapses is magnified in the bottom panel. Scale bars, top, 10 µm; bottom, 1µm. b. Exemplary images of synapses labelled as in a, but after X10 expansion. The overview image (top) is a maximum-intensity projection of a 77-slice z-stack spanning 15 µm (200-nm step size) in terms of physical size, or 1.5 µm (20-nm step size) downscaled to the sample's size before expansion. The magnified view below shows a maximum-intensity projection of the three slices of best focus for the boxed region. Adapted from (Truckenbrodt et al., 2019)

Computation methods in biological analysis

Computational microscopy bioimage analysis has long been established as a tool for protein aggregation characterization. Since intensity or morphologic values can be assessed using computational analysis in a high-throughput manner. The general workflow involved in the computational processing of microscopy bioimages is described in Figure 11.

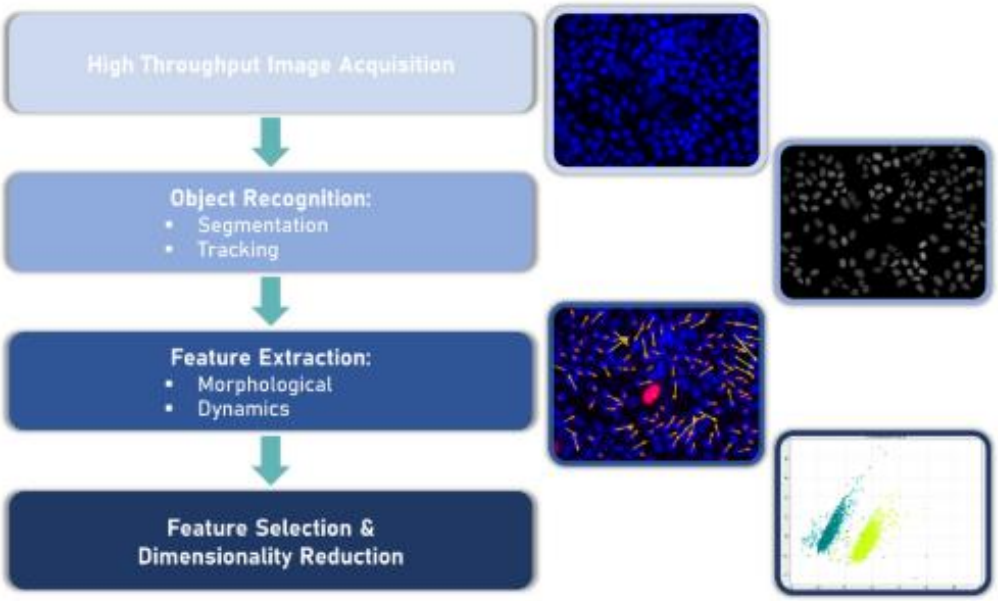

Figure 11**. Workflow for the digital analysis of microscope images**. Adapted from (Grys et al., 2017)

The use of manual analysis has been the most used way to get information from the images (Patrick Weish, Diana F. Lázaro, Luís Palmares, Patrícia I. Santos, Christine Stadelmann, Günter U. Höglinger, Silvio O. Rizzoli, n.d.). The use of simple and reduce the effect of the user will be a good advantage to create a more homogeneous characterization.

As an alternative to manual analysis, it is less cumbersome, more objective, less biased, and large volumes of image data can be processed efficiently, possibly minimising erroneous conclusions stemming from outlier behaviour. Several possibilities could be used to solve the problem like a simples threshold (Perkins, 1980) or Otsu threshold (Zhang & Hu, 2008) but the arise of machine learning came to revolute the way of segmentation (Schmidt et al., 2018; Weigert et al., 2020).

Segmentation methods

Once biological data is imaged, namely regarding monolayers of cells or tissues, segmentation and tracking of cells or structures the following step in the analysis. For segmentation, two main tasks are required – structure discrimination from the background and separation.

These tasks will usually either require high levels of human input or high levels of configuration and customization for each individual experiment. This is antagonist to the development of high-throughput methods of segmentation. Some of the most popular bioimage processing tools (Wiesmann et al., 2015) which help with automation include Fiji (Schindelin et al., 2012), CellProfiller (McQuin et al., 2018) and Icy (de Chaumont et al., 2012).

Two main approaches are used for segmentation. The edge-based approach locates discontinuities in the image, assumed to correspond to the border of the ROI; the region-based approach, alternatively, achieves segmentation by assuming homogeneity of the ROI (Preim & Bartz, 2007). Methods commonly used for segmentation of fluorescent microscopy image data include filtering (gaussian blur for smoothing, variance for edge enhancement), which is often a pre-processing stage along with techniques for Signal-to-Noise Ra- tio (SNR) enhancement; global or local adaptive thresholding (Otsu, 1979); watershed (Vincent & Soille, 1991); or active contour (Kass et al., 1988) algorithms. While many tools are available, and even if image data collection is performed to the best of the available conditions, segmentation will usually involve manual adjustment of parameters, either according to the dataset or even within one dataset, due to heterogeneity of the samples or the occurrence of technical artifacts (Dima et al., 2011).

Ideally, a segmentation should be able to properly segment the structure without the need for manual adjustment, regardless of the image type or experimental conditions - fully automated, generic and robust. Modern approaches to the segmentation problem often make use of machine learning strategies (Kan, 2017), or even deep learning (Ronneberger et al., 2015). While these models have been shown to perform better than other classical methods (Caicedo et al., 2019), annotation of datasets and training of the net is burdensome and technical variability in data collection continues to be a challenge due to overfitting

2. Materials and Methods

The workflow can be divided in 4 steps: Cell culture, Transfection and Immunocytochemistry, Imaging and Digital Processing (Figure 12).

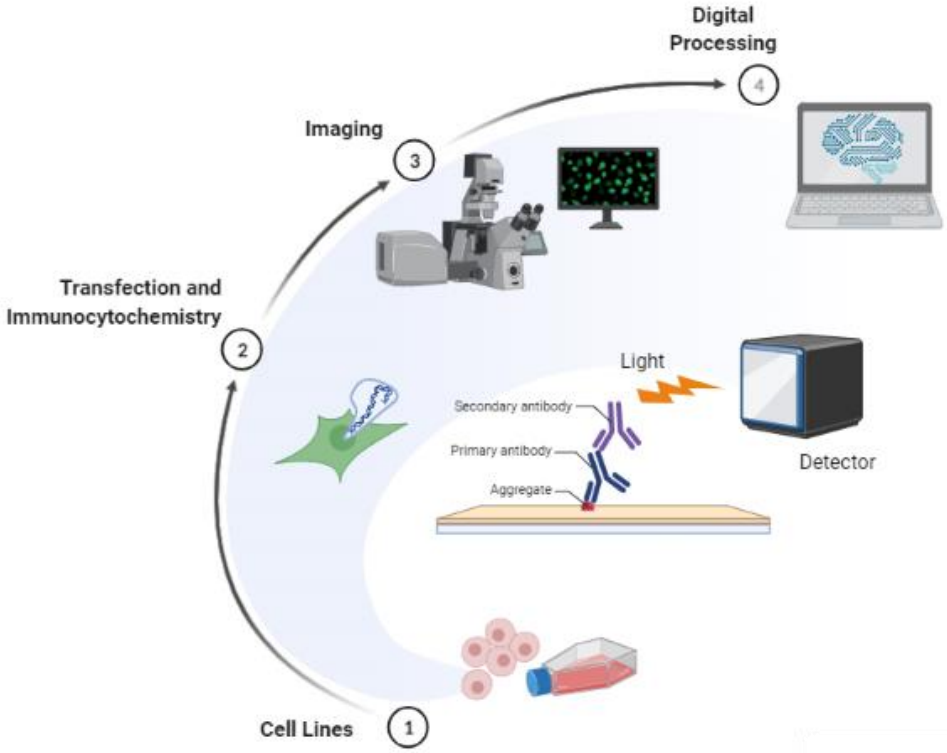

Figure 12. **Overview of the experimental workflow.**

The transfection was developed in several cell lines (HEK-Kidney epithelial cells- and H4- Human neuroglioma cells-). After transfection, immunocytochemistry was done to stain the proteins of interest. Then, imaging those cells using confocal, STED and Expansion microscopy to finally process those images digitally to obtain different variables.

Preparation and acquisition of biological data

The collection of the biological data can be divided into four main stages: Cell culture, cell transfection, immunocytochemistry, and imaging. Each of these sections will be described in detail in the sections below.

Cell Culture

There were two types of cells to study the aggregation models. HEK were used to study the aggregation of Sph1-GFP while H4 were used to study the SynT WT with Sph1 aggregation model.

HEK cells are cultured in DMEM medium®(Life Technologies) supplemented with 10% Fetal Bovine Serum and 1% Penicillin /Streptomycin. The cells were grown at 37◦C in an atmosphere of 5%CO2.

Human neuroglioma cells (H4) were maintained in OPTI-MEM®(Life Technologies) supplemented with 10% Fetal Bovine Serum and 1% Penicillin/Streptomycin. The cells were grown at 37◦C in an atmosphere of 5%CO2.

Transfection

Metafectene Transfection

This method of transfection was used exclusively in HEK cells. 1µg of DNA (Sph1 tagged with EGFP) and 50µL of OPTIMEM® (Life Technologies) have been mixed. Meanwhile, in another Eppendorf, 2µg of Metafectene and 50µL of OPTIMEM have been mixed. After 5 minutes, both solutions are mixed and left to rest for 20min (Figure *13*)(Biontex, n.d.).

Finally, 100µL of the solution is mixed in a 12 well-plate for at least 24h. 24h later, the medium of the cells is changed to the cell culture medium. After 48h, the transfection is stopped by fixation with 4% paraformaldehyde (PFA).

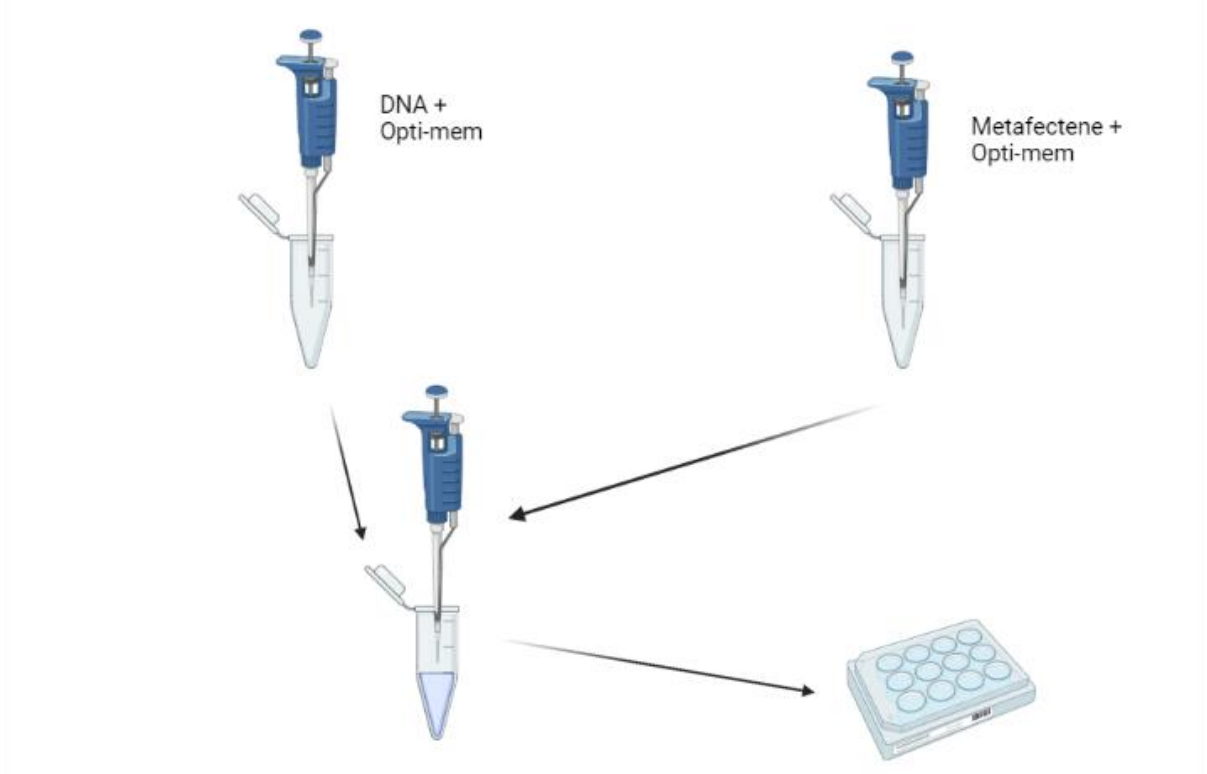

Figure 13. **Schematic representation of the steps involved in Metafectene transfection.** In the first Eppendorf, the solution of DNA and Opti-mem are mixed with the solution of Metafectene and Opti-mem.

Fugene Transfection

This method was used for the H4 cells. As described by the manufacturer, 100uL of OPTIMEM®(Life Technologies) and 6uL of Fugene (Promega). After 5 min,1ug of DNA (SynT WT and Sph1) was added

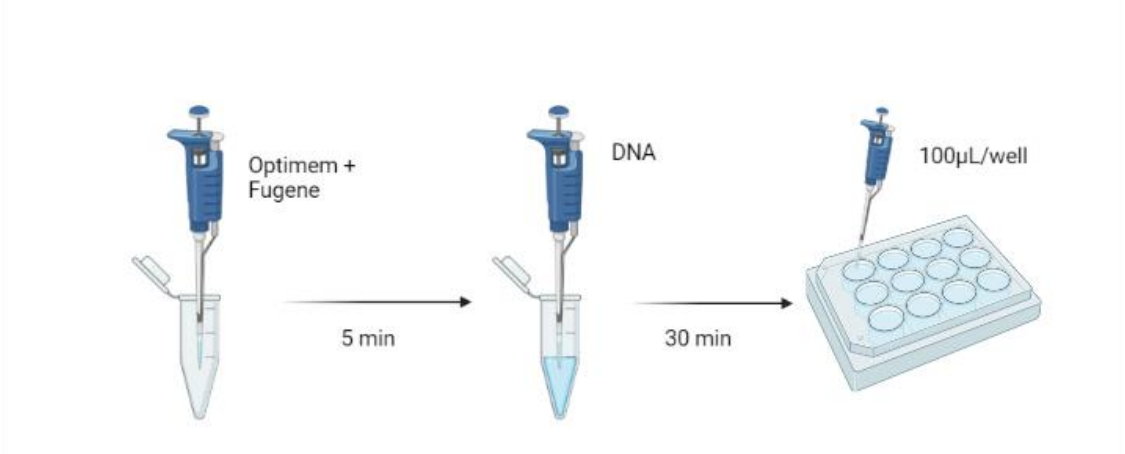

Figure 14. **Schematic representation of the Fugene Transfection**. It is mixed the Opti-mem and the Fugene. After 5min, the DNA is added.

and left to rest for 30min and, finally, 100µL of the solution was mixed in a 12 well-plate for 48h (Figure 14).

Immunocytochemistry

After the transfection and the fixation of the cells with PFA 4%, were washed three times with PBS1x around 5min in the shaker. Then, it is incubated with Tritton-1x in PBS, shaking.

After 10min, a blocking solution (3% BSA in PBS 1x) was added and left it at Room Temperature (RT) on the shaker. In that hour, the solution with the first antibody is prepared where depending on the type of microscopy used the concentration can change (1:1000 in Confocal and STED Microscopy and 1:100 in Expansion Microscopy), the solution is prepared in the blocking solution previously prepared. After the incubation overnight of the primary antibody (concentrations and markers are shown in Table *1*), the cells are washed with PBS1X three times around 5 min each wash.

Table 1. **Antibodies used in immunocytochemistry protocol.**

		Aggregation model	
Type of Microscopy		**Sph1**	**SynTWT+Sph1**
Confocal	1º AB	---	1:1000 Anti αSyn Mouse (BD, USA) + 1:1000 Anti V5 Rabbit (Abcam, UK)
	2º AB	---	1:1000 Alexa Fluor 488 donkey anti-mouse IgG (Thermo Fisher Scientific, USA) + 1:1000 Alexa Flour 555 goat anti-rabbit IgG (Invitrogan, USA)
STED	1º AB	---	1:1000 Anti αSyn Mouse Mouse (BD, USA) + 1:1000 Anti V5 Rabbit (Abcam, UK) + 1:1000 Anti α-tubulin Rat (SySy, Germany)
	2º AB	---	1:1000 Alexa Fluor 594 goat anti-rabbit IgG (Thermo Fisher Scientific, USA) + 1:1000 Abberior Star 635P goat anti-mouse IgG (Abberior, Germany) + 1:1000 Alexa Fluor 488 donkey anti-rat IgG (Thermo Fisher Scientific, USA)
Expansion	1º AB	1:100 Anti GFP Mouse (Roche, Switzerland)	1:100 Anti αSyn Mouse Mouse (BD, USA) + 1:100 Anti V5 Rabbit (Abcam, UK)
	2º AB	1:100 Alexa Fluor 488 donkey anti-mouse IgG	1:100 Alexa Fluor 488 donkey anti-mouse IgG (Thermo Fisher Scientific, USA) + 1:100 Alexa Flour 555 goat anti-rabbit IgG (Invitrogan, USA)

		(Thermo Fisher Scientific, USA)	

Meanwhile, the secondary antibody solution (Concentrations and markers are shown in Table *1*) is prepared with the blocking solution with different concentrations of antibody (1:1000 in Confocal and STED microscopy and 1:100 in Expansion Microscopy). The cells were incubated for 1h at RT on the shaker and then, the cells were washed again with PBS 1x three times around 5min each wash. The entire scheme of the antibodies can be seen in Table *1* and Figure *15*.

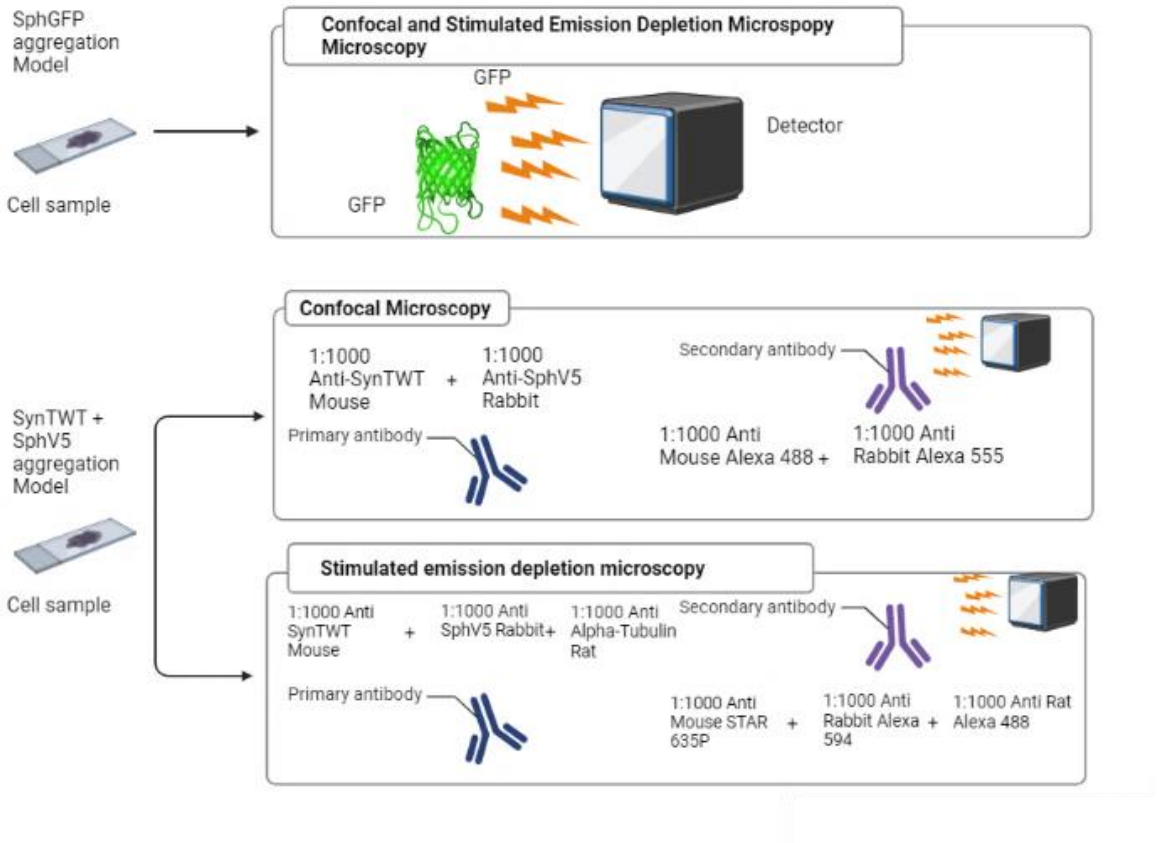

Figure 15**. Graphic display of the antibodies used in immunocytochemistry.**

As the nucleus is one region of interest, after the final step, the DAPI solution (1:1000) was added for 5 min and then washed again with PBS1x.

Mowiol is used to mount the slides and, finally, the slides are left to dry at RT covered from the light.

Confocal Microscopy

Imaging was conducted on a ZEISS LSM 800 using 100X and 1NA objective. Each collected image represents a range of z-slides (32 slices in Sph1-GFP and 24 slices in SynTWT+Sph1aggregation model) with the information of the entire cell. The dimensions of each image are 2048x2048 px (30,1 nm in Sph1-GFP aggregation model and 41,2 nm in SynTWT+Sph1 aggregation model).

Each aggregation model was imaged in different experimental groups.

There are 3 experimental groups to consider for the Sph1-GFP aggregation model:

- Negative Control, without any transfection, just adding DAPI for imaging the nuclei.
- Positive Control, which was performed with transfection of the PeGFP plasmid. Nuclei were stained with DAPI.
- Experimental groups (n=3 – 50 cells per n), which were transfected with Sph1-GFP using the Metafectene method. Nuclei were stained with DAPI.

There are 7 experimental groups for the SynTWT+Sph1 aggregation model:

- Negative Control without any transfection. Nuclei were stained with DAPI.
- Positive Control, with transfection of pcDNA to evaluate the transfection process.
- The antibodies were also tested during the protocol:
    - Group 1 with just the Primary antibody and the group 2 with only secondary antibody
    - Two different imaging were performed to have both antibodies separated. Using just the Primary antibody and secondary to SynT WT (group 3) and another group to evaluate the Sph1 (group 4).

STED Microscopy

The imaging of each model was conducted in a different setup due to physical limitations of the lasers and the goal of resolution in z axis.

Imaging the Sph1-GFP aggregation model was conducted on a Custom setup described in (Willig et al., 2014) using 100X and 1 NA objective. This setup was based on (Wegner, Ilgen, Gregor, Van Dort, et al., 2017). The dimensions of each image are different for each cell (20nm/px). Each image collected represents a range of z-slides (200 nm/px) to have information of the entire cell.

Imaging the SynTWT+Sph1 aggregation model was conducted on a Custom setup (Wegner, Ilgen, Gregor, Van Dort, et al., 2017)(van Dort, 2018)) using 100X and 1.4 NA objective (HCX PL APO 100x/1.40 OIL STED, Leica Microsystems, Wetzlar, Germany). Each image collected represents a range of z-slides (100nm/px) to have information of the entire cell. The dimensions of each image are different for each

cell (40nm/px). This model had the advantage of using a 3D STED which helps in the resolution in the z direction.

Expansion Microscopy

The expansion protocol was performed as described in (Truckenbrodt et al., 2019). After immunocytochemistry, the samples were incubated overnight with 500µl of Anchoring buffer (1x PBS + 0.1mg/ml Acryloyl-X (Life Technologies, Carlsbad, CA, USA)) at RT.

The day after, the samples were washed with 1x PBS three times for 5 min, and the polymerization solution was applied. For the X10 gelling solution, 33% (w/w) of high purity sodium acrylate (SA) and N,N-dimethylacrylamide acid (DMAA) monomers solution was dissolved at a molar ratio of 4:1 (DMAA:SA) in ddH2O. The polymerization solution was bubbled with nitrogen gas for ~40 min at RT. In a separated tube, potassium persulfate (KPS) (0.036 g/ml stock of KPS) was prepared at 0.4 molar% relative to the monomer concentration and mixed with the DMAA+SA solution. Another 20 min of bubbling with nitrogen gas was performed in a mix of ice + water to keep the temperature homogeneous and closer to 0ºC as possible. For 1ml of gelling solution, 4µl of N,N,N',N'-tetramethyl-ethane-1,2-diamine (TEMED) was added. Then, 60µl of the solution was applied into the chamber prepared previously according to (Truckenbrodt et al., 2019). The polymerization took between 1-3 days, after that period.

Then, the gel from the polymerization was incubated overnight in a humid chamber with digestion buffer (50mM of TRIS + 800 mM guanidine HCL + 1mM EDTA + 0.5% (vol/vol) Triton X-100) and Proteinase K in a concentration of 1:100.

Imaging was performed on a Zeiss Axio Observer (ZEISS, Germany) with an Air 20X objective and 0.25 NA. The estimation of the Expansion Factor was done using the expression (Equation (4)), which was calculated using 50 nuclei of pre-expansion cells and 50 nuclei of post-expansion cells.

$$Expansion\ Factor = \frac{\sqrt{\sum Area_{Post}}}{\sqrt{\sum Area_{Pre}}}$$ (Truckenbrodt et al., 2019)

(4)

Digital Processing

The Processing of the data can be divided in four steps (Figure 16Figure *16*): creation of 3D matrix to each channel of interest; the 2D segmentation using the Stardist Network (Schmidt et al., 2018; Weigert et al., 2020) were done for each slice , then a relationship between the segmented areas was created to configure the object- aggregate- and finally the statistical analysis taking the number of the

aggregates per cell and the volume of each aggregate. In SynTWT+Sph1 aggregation model, the colocalization was a variable to analyse.

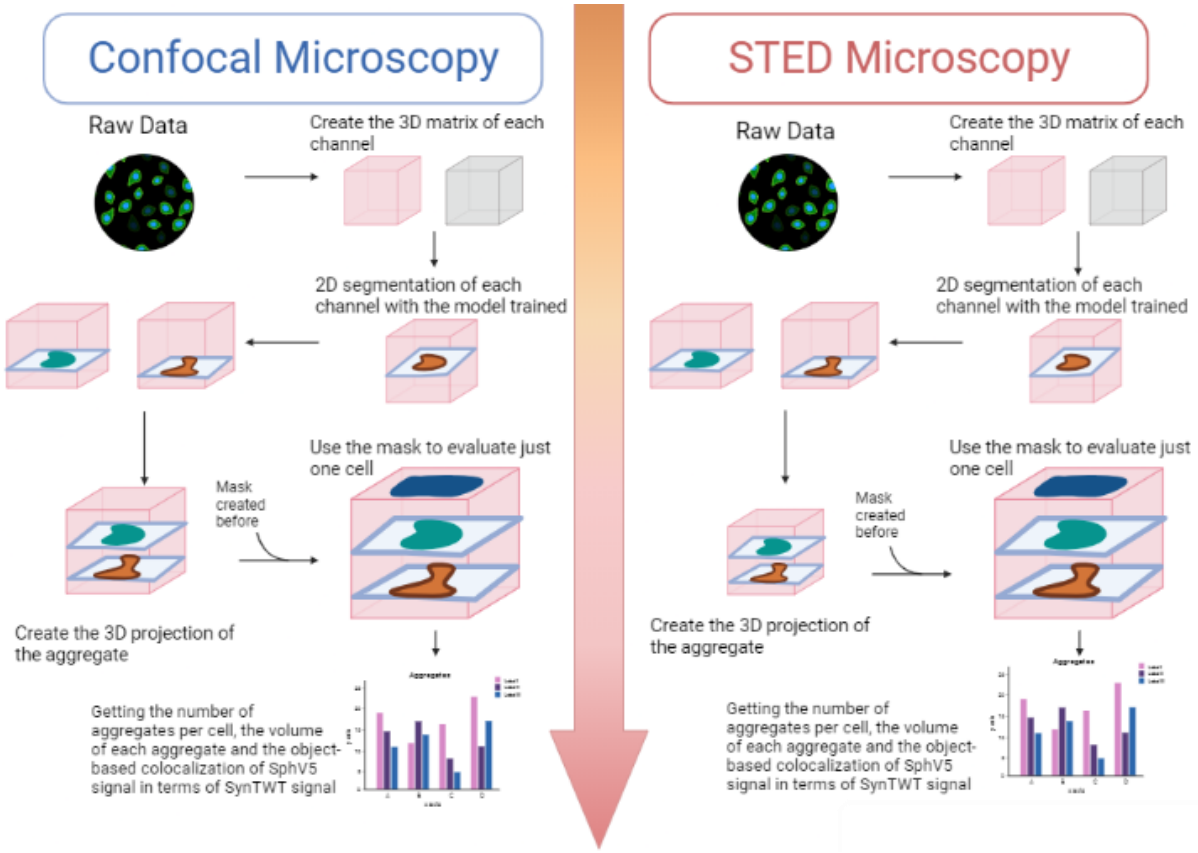

Figure 16**. Workflow of the digital processing**. Firstly, the data of each channel is converted into a 3D matrix to then, be segmented with a custom trained model to the region of interest. After segmentation, a relationship between the segmented areas is created using the fact of continuity of the aggregates between the adjacent slices. Lastly, 3D projections and number of aggregates per cell, volume of each aggregate and colocalization (just for SynTWT+Sph1 aggregation model) are developed.

Deep Learning Algorithm

Model training was performed by recurring to pictures given by Liana Shvachiy of the same aggregation model used in the experimental data (150 for SynTWT+Sph1 aggregation model and 87 pictures to Sph1-GFP aggregation model). The channel of interest needs to be taken in consideration due to heterogeneity between the channels, in other words, for every channel a model must be created in separate. Then, the model was used to segment in 2D.

Creation of the mask

To have one cell per image, the pre-analysis was performed to create masks for each picture to make sure that just one cell was taken in consideration.

Relation of segmentation

The 2D segmentation of each layer was related though masks with a previous list of objects already taken as possible aggregates. Then, the fact that each aggregate needed to be convex and continuous in the z axis was taken into consideration. In each layer, there are3 possibilities: the segmented area can intersect with just one possible aggregate; the segmented area can be alone and no interaction with any possible aggregates; or the segmented area can interact with more than one aggregate. In the first two options, the solution looks obvious, when there is an interception, a new possible aggregate is added to the list, when there is just one intersected aggregate, then the volume of that layer is added to that object with the replacement of the new mask. When there is more than one possible aggregate, the volume of all possible aggregates is added, and it is by replacing those possible aggregates by one with the merge of those aggregates. In the end of the process, the possible aggregate with just one layer was removed because of the low probability of having so small aggregates.

Colocalization

In the SynTWT+Sph1 aggregation model, an object-based colocalization was performed where it was analysed the intersection of the Sph1 over the SynTWT signal. This value was removed in each layer using the predicted from the model. Then, for each image (and cell) the average colocalization and the maximum was taken as results.

Statistical Analysis

The average and standard deviation of the volume of aggregates was calculated. The average and standard deviation of the number of aggregates per cell and average and standard deviation of volume of aggregates per cell. In SynTWT+Sph1 aggregation model, the average and standard deviation of mean colocalization and maximum colocalization was analysed.

Data collection

Segmentation and analysis rendered a total of 363 cells. The distribution of cells per type of microscopy and aggregation model can be seen in Table *2*. Collection of ExM was used simply to create the Maximum Intensity Projection through the phase cross correlation alignment.

Table 2. **Number of the images taken in each microscopy and aggregation model.** The difference of the number of images taken is related with the time to record the images.

Type of Microscopy	Sph1-GFP Aggregation Model	SynTWT+Sph1 Aggregation Model
Confocal Microscopy	150	150
STED	33	30
ExM	150	75

3. Results

Qualitative analysis of Imaging in Sph1-GFP and SynT+Sph1 aggregation models

To evaluate the aspect of the image to ensure that the analysis is performed in a cell with aggregates, the maximum intensity projection (MIP) was created in each aggregation model and type of microscopy. Imaging from confocal and STED microscopy was done, obtaining representative MIP images from each aggregation model and type of microscopy (Figure 17 and Figure 18)

In Figure 17a, MIP of confocal images of the Sph1-GFP aggregation model in HEK cells. In green, the signal from GFP is visible with the presence of aggregates. Images were taken at 100x magnification. Scale bar is 10µm. In Figure 17b, MIP of STED images of the Sph1-GFP aggregation model in HEK cells. In green, the signal from GFP is visible with the presence of aggregates. Images taken at 100x magnification. Scale bar 10µm. These were the images used for further analysis using computational tools. According to the Figure 17, it is expected to have similar results in both types of microscopies where large aggregates and low numbers of aggregates are expected.

As for SynT WT + Sph aggregation model, different antibodies were used because of the technique applied. In confocal microscopy (Figure 18a), the αSyn signal was collected at 488nm, the Sph1 signal was collected at 555nm and DAPI at 405nm of wavelength. In STED microscopy (Figure 18b), the αSyn

signal was collected at 635nm, the Sph1 was collected at 594nm and DAPI at 488nm of wavelength. In Expansion microscopy, the collection of the signals was similar to the one used in confocal, however using 20x magnification in an epifluorescence microscope.

As shown in the previous work from the group, in the SynTWT+Sph1 aggregation model (Figure 18) the cells display a different aggregation pattern. That would be the first impression to evaluate the difference between the Confocal and STED microscopy.

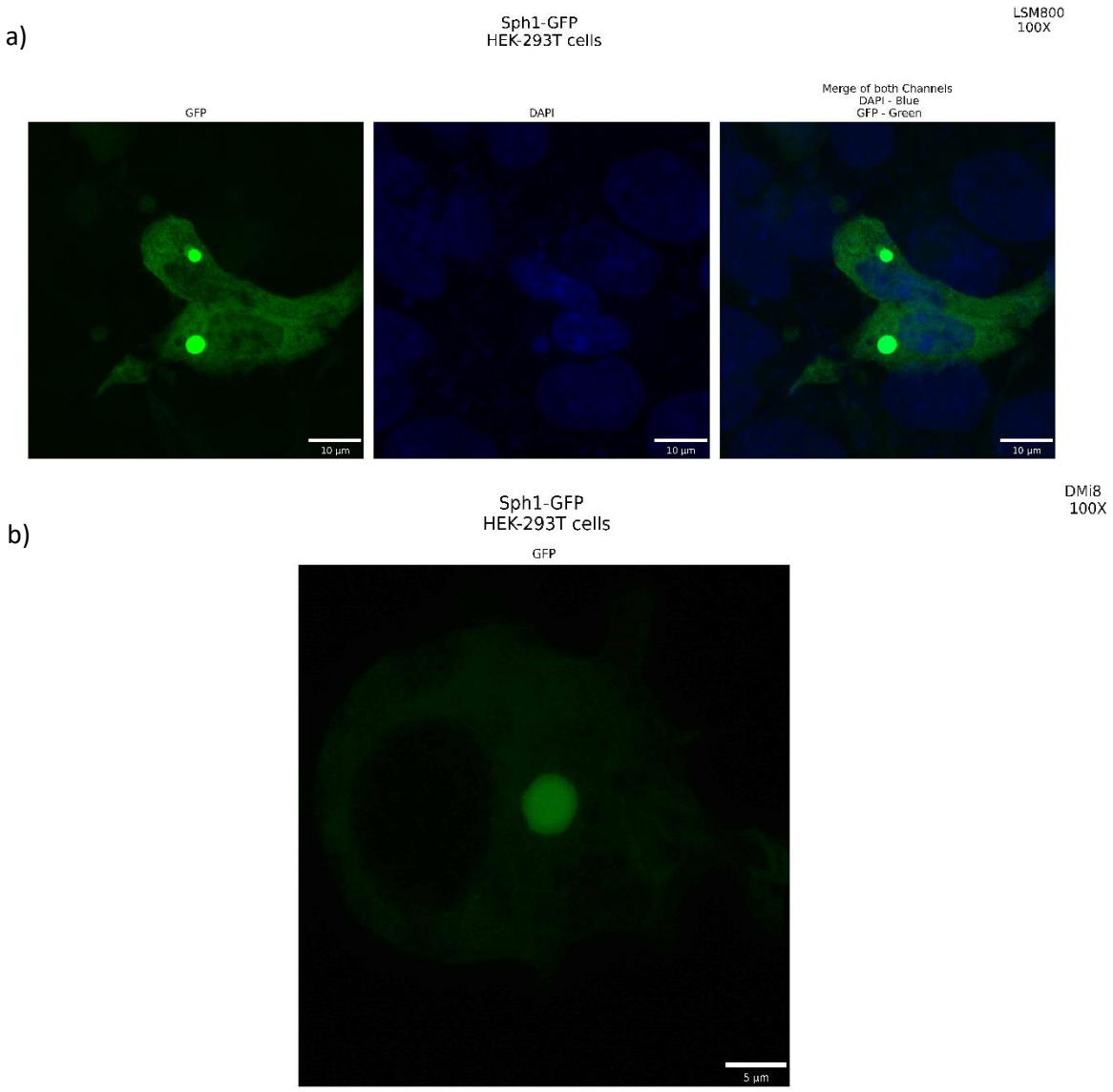

Figure 17. **Representative MIP images from the SphGFP model.** a) MIP taken in consideration as a standard image from confocal microscopy. Images taken at 100x magnification. Scale bar 10µm. b) MIP to taken in consideration as a standard image from STED microscopy. Images taken at 100x Scale bar 5µm.

In the Expansion Microscopy data, the full analysis was not complete due to time constraints. Meanwhile, the alignment of the images regarding the Z axis using phase cross correlation function was performed to get the better approach and create a similar 3D matrix as in the other types of microscopies.

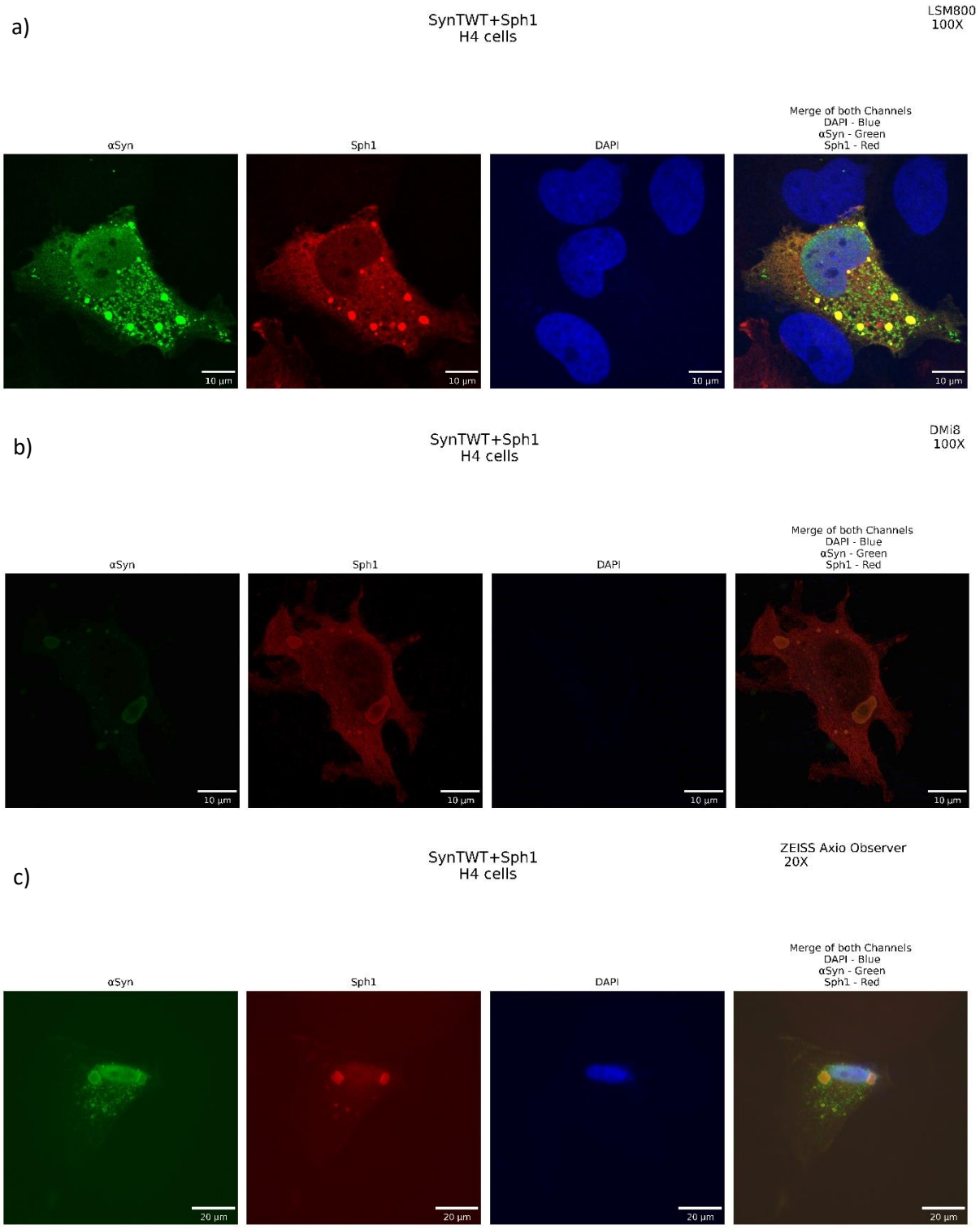

Figure 18. **Representative MIP images from SynTWT+Sph1 aggregation model. a**) MIP taken in consideration as a standard image from confocal microscopy. Images taken at 100x magnification. Scale bar 10µm b) MIP taken in consideration as a standard image from STED microscopy. Images taken at 100x magnification. Scale bar 10µm c) MIP taken in consideration as a standard image from ExM images taken at 20x magnification. Scale bar 20µm.

2D segmentation in each slice of the image

The following section gives an overview of the type of segmentation in each type of microscopy and model in question. The evaluation of the trained model was performed using the intersection over union parameter. The Sph1-GFP model had a precision of 86.67% in the validation images taken from the batch of trained data. The SynTWT+Sph1 has two models to be evaluated according to the signal, in the SynTWT (green channel), a precision of 76.92% was achieved and in the Sph-1 (red channel) a precision of 90.91% was obtained.

The segmentation is an important part of the results since it has a direct factor in the volume of the aggregate due to the fact of summing each volume of the segmented area.

Segmentation in Sph1-GFP aggregation model

The number of z slices in each type of microscopy was different due to the resolution available to achieve and the setup used, but the segmented shape, as previously explained in the methods section, follows the convex-polygon shape (Figure 19 and Figure 20).

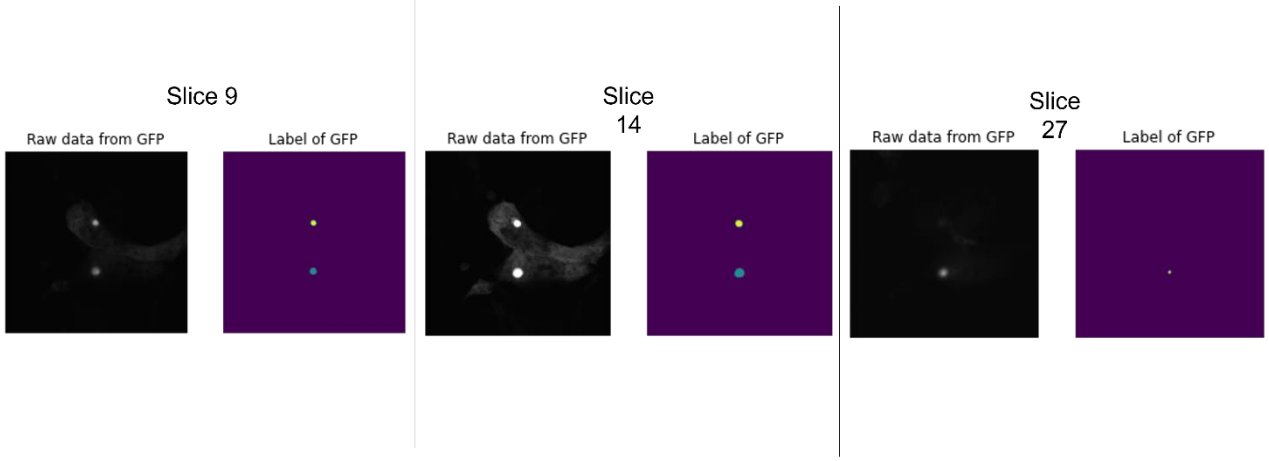

Figure 19. **Raw image(left) and Segmented areas(right) in some slices from confocal images in Sph1-GFP aggregation model.** The raw and segmented images from the slice 9(left),14(middle),17(right) in the MIP image presented before.

The segmentation was done recurring to a custom trained model from images taken previously to give the label image and the raw channel. In Figure 19, the 2D segmentation of the Slices 9,14 and 27 are shown, respectively, from one image used in this work. If we compare the left (raw data) and right (segmentation), the segmentation data looks very promising in the central slice which then could be improved in the top and bottom slices.

Using the same model trained for the confocal microscopy images, the segmentation from STED images looks similar with the previous one with circular shapes (Figure 20). The hypothesis of circular

and round aggregates was tested as seen by the segmented areas that seem to be bigger in terms of the area in the most central slices of the image.

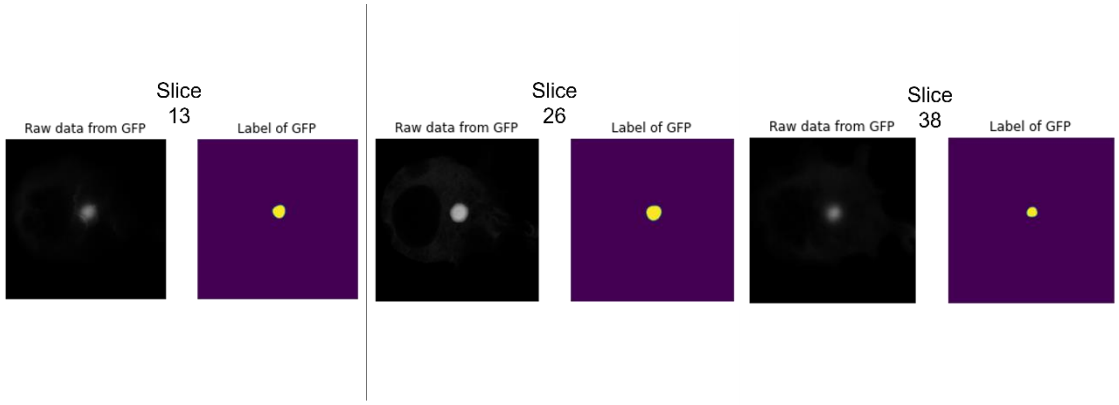

Figure 20. **Raw image (left) and Segmented areas (right) in some slices from STED images in Sph1-GFP aggregation model.** The raw and segmented images from the slice 13 (left),26 (middle),38 (right) in the MIP image presented before.

Segmentation in SynTWT+Sph1 aggregation model

To compare and create a volumed shape of the aggregate, the segmentation was an important step. Using a previously trained model for each channel of interest, the segmented areas are shown in Figure 21(Confocal Microscopy) and Figure 22(STED Microscopy).

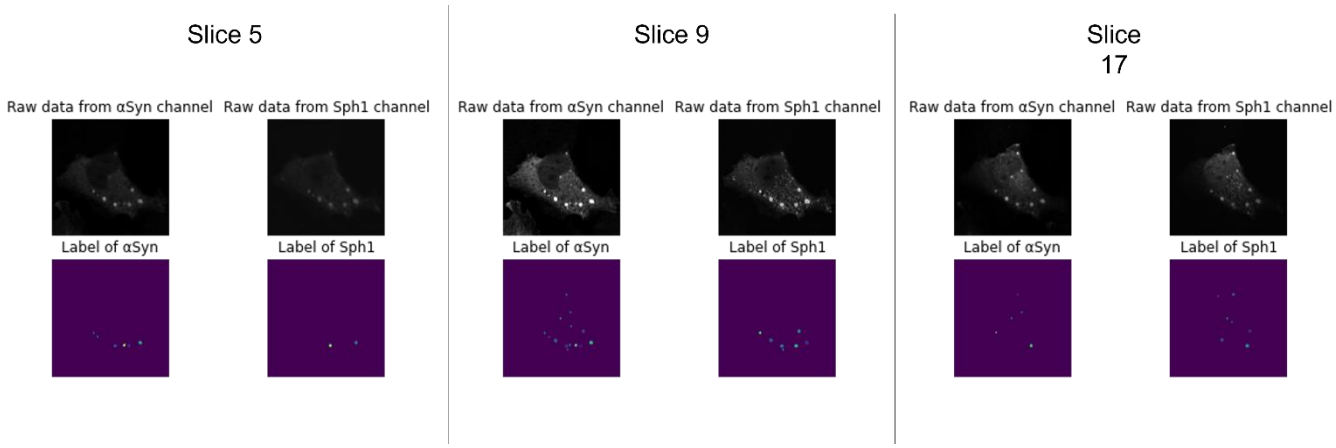

Figure 21. **Raw images (top) and Segmented areas (down) in some slices from confocal images in SynTWT+Sph1 aggregation model.** Each slice has two segmentations due to the fact of there are two channels of interest (SynT channel on the left and SphV5 on the right). The raw and segmented images from the slice 5 (left),9 (middle),17 (right) in the MIP image presented before.

Having the Figure 22(Slice 12,30,39) in mind from STED microscopy, it is clear that not all the possible aggregates were predicted. Although, the shapes of those areas are well defined.

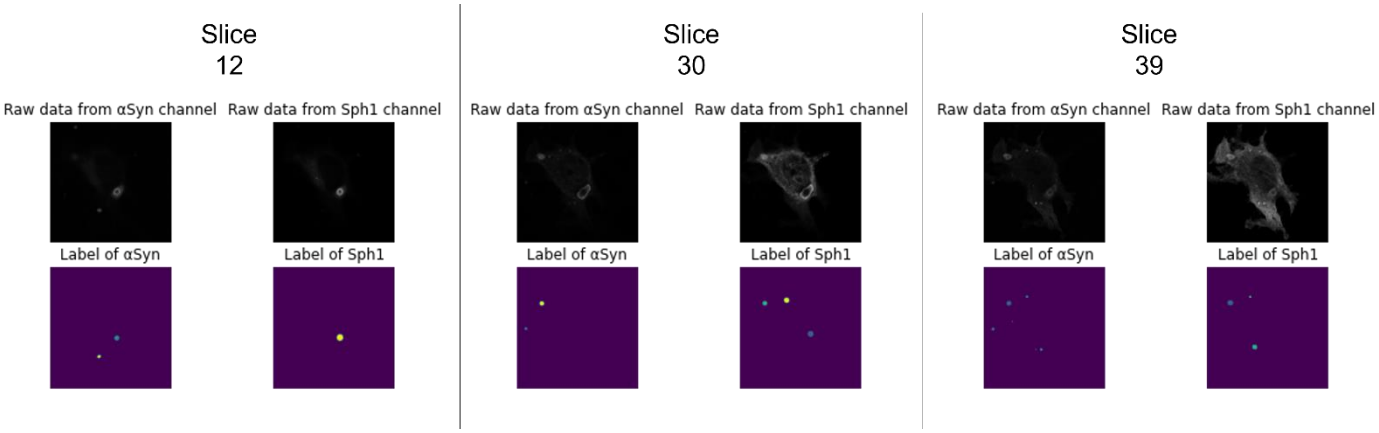

Figure 22. **Raw images (top) and Segmented areas (down) in some slices from STED images in SynTWT+Sph1 aggregation model.** Each slice has two segmentations due to the fact of there are two channels of interest (SynT channel on the left and Sph1 on the right).

3D projection and Statistical Values

This section takes in consideration some images of each model and type of microscopy as a 3D projection to have a better understanding of the spatial location of aggregates that are in interaction with each other.

According to the literature, a small number of aggregates with a high volume is expected. In Figure *23*, the 3D projections from the images segmented before (Figure 19) clearly provide the expected results regarding the number and size of the aggregates in Sph1-GFP aggregation model on confocal microscopy.

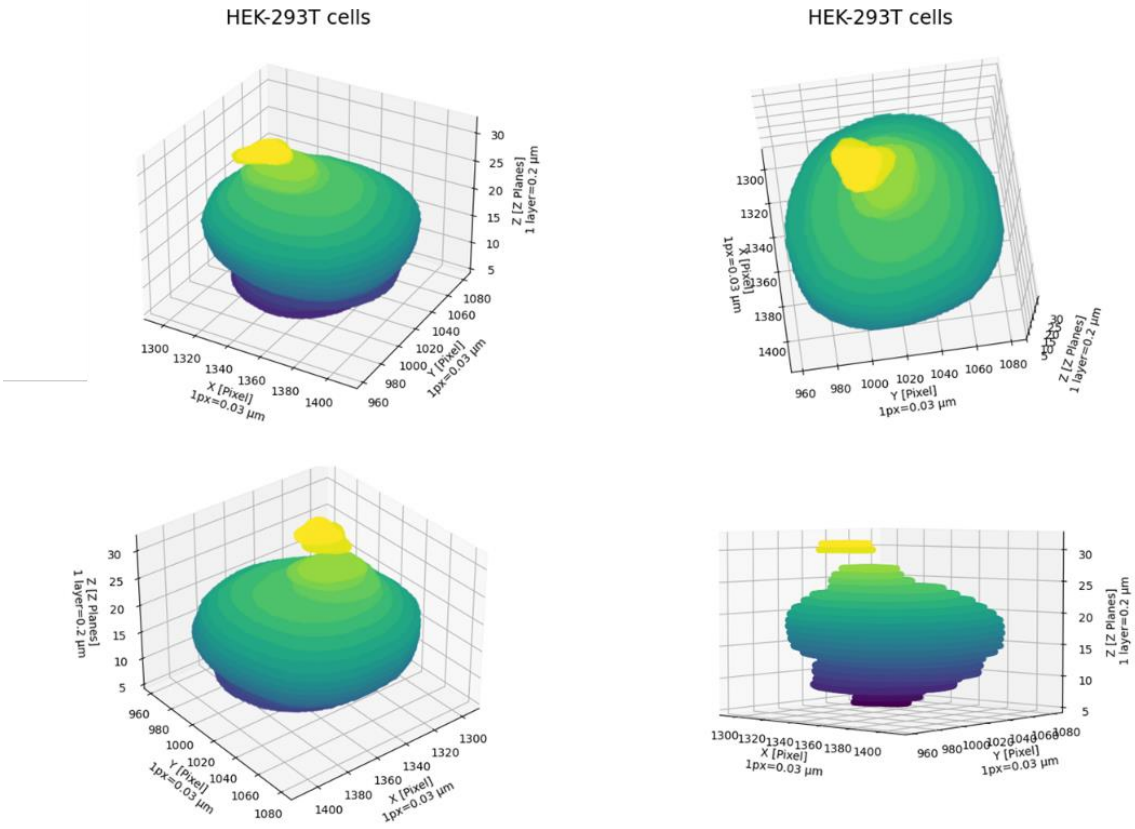

Figure 23. **Several views of the 3D projection from confocal microscopy in the Sph1-GFP aggregation mode**l. These views are the analysis of the segmented areas and MIP image from confocal microscopy and Sph1-GFP aggregation model.

3D projections from confocal images provide the large aggregates in most of the slices of the image and large volume as it can be confirmed by the x and y axis. Although, in Figure *23*, two aggregates were segmented, one with a large volume and a smaller one on the top of the big one.

The analysis from STED images provides similar results in terms of the number of aggregates (Figure 24). As a result of this analysis, just one aggregate occupying the most of slices of the image is segmented.

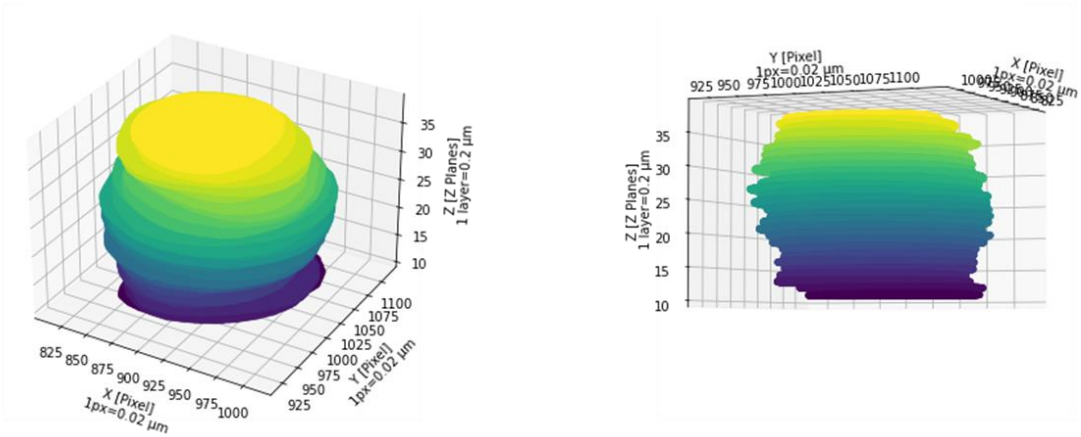

Figure 24. **Several views of the 3D projection from STED microscopy in the Sph1-GFP aggregation model.**

These views are representative analysis from images from STED microscopy regarding the Sph1-GFP aggregation model.

Both types of microscopies resulted in big aggregates with a convex and bull shape. The difference between both types of microscopies does not seem to be significant.

In the SynTWT+Sph1 aggregation model, the 3D projection shows both segmented aggregates of SynTWT channel (green colormap) and the Sph1 (red colormap).

As seen in the segmented slices previously, it is expected to have more aggregates than the Sph1-GFP with a smaller size. In Figure *25*, the 3D projection from confocal microscopy in the previous MIP pictures and segmented slices show the results expected with higher quantity and lower size aggregates.

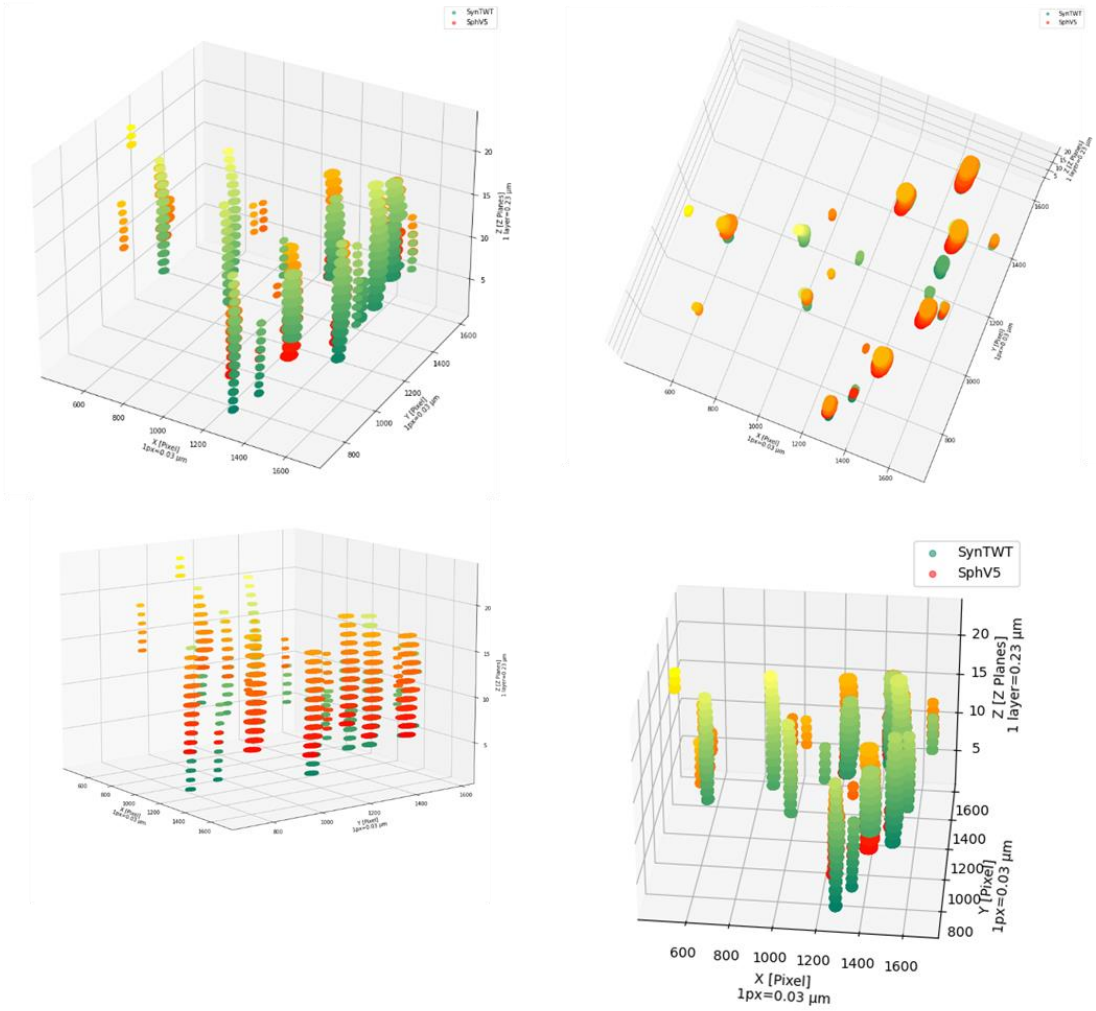

Figure 25**. Several views of the 3D projection from confocal microscopy in the SynTWT+Sph1 aggregation model.** These views are the analysis of the segmented areas and MIP image from confocal microscopy and SynTWT+Sph1 aggregation model.

After analysis of the STED images to the same aggregation model, where the green colormap represent the SynTWT signal and the red colormap represent the Sph1 signal, the results from 3D projections provide us the expected size of the aggregates (Figure 26). The higher number and small size of the aggregates looks similar with the results from confocal microscopy.

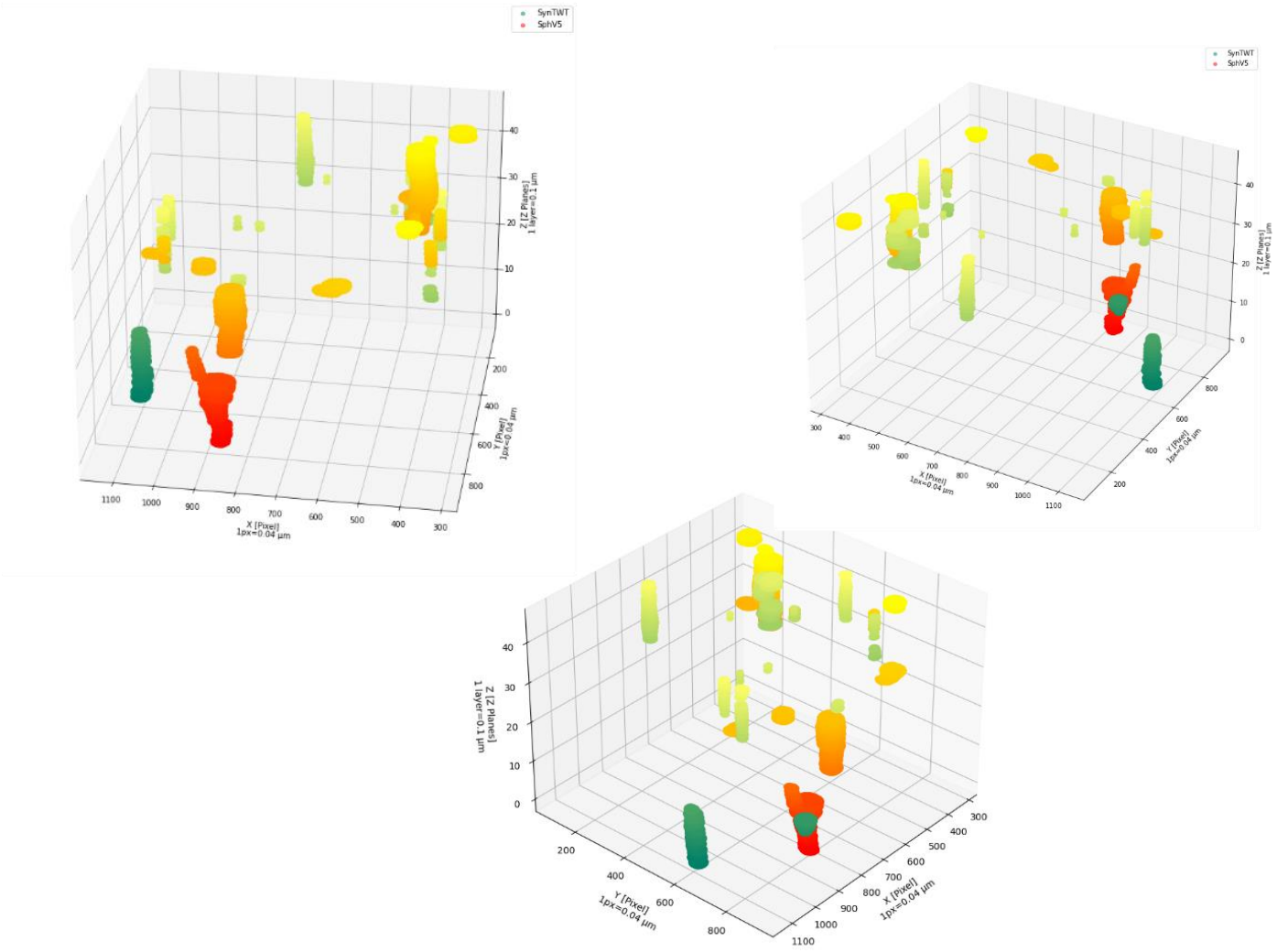

Figure 26**. Several views of the 3D projection from STED microscopy in the SynTWT+SphV5 aggregation model.** These views are the analysis of the segmented areas and MIP image from confocal microscopy and SynTWT+SphV5 aggregation model.

There are some differences regarding the shape of the aggregate comparing both microscopy techniques in the same aggregation model. The number of aggregates looks similar although with a different spatial localization of each protein aggregate. Analysing the possible interaction between the SynTWT and Sph1 proteins, both types of microscopies provide some evidence that there is colocalization between the proteins.

To test the hypotheses and discuss some results, statistical analysis using several metrics was performed. For the Sph1-GFP aggregation model, a box plot of the results of 50 images (one N), the average and standard deviation of the aggregate volume per N and an average of the experiment were performed for each type of microscopy (Figure 27 correspond to confocal microscopy and Figure 28 correspond to STED microscopy).

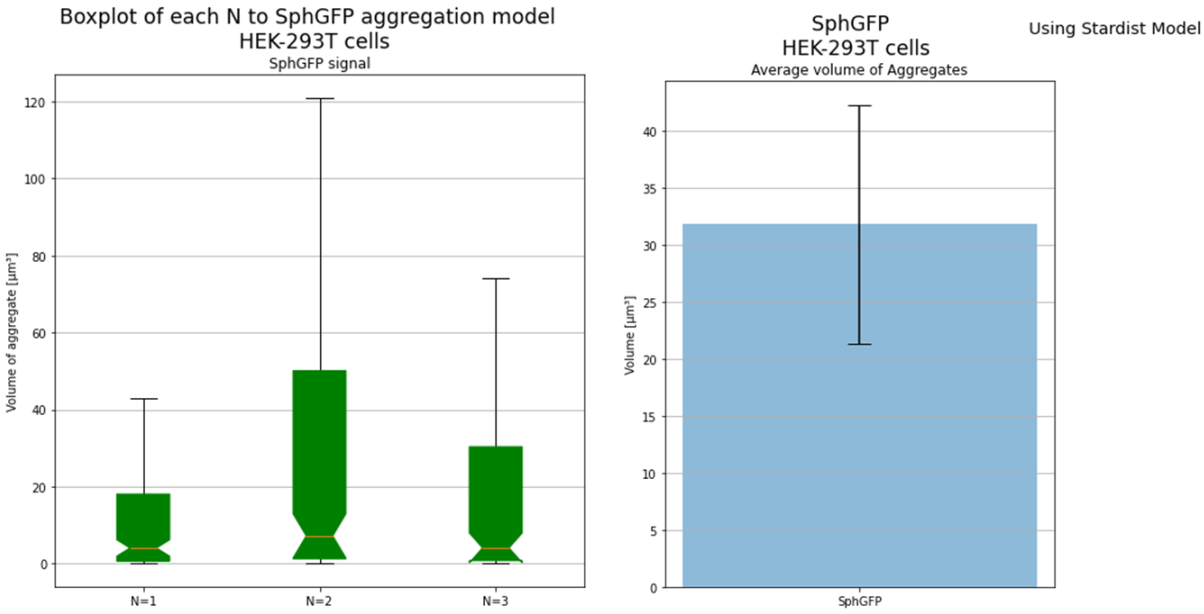

Figure 27. **Boxplot and the average volume of aggregates using confocal microscopy in the Sph1-GFP aggregation model.** The boxplot represents the median and the range of values in each N (Left). The average and standard deviation volume of the aggregates was created in a bar plot (right).

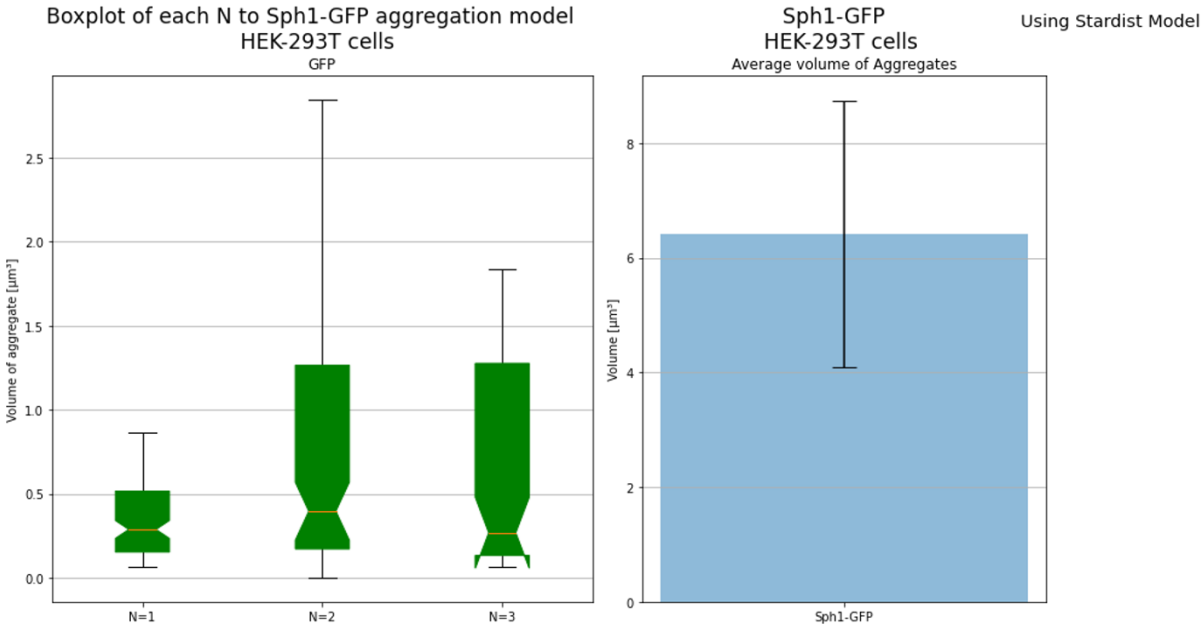

Figure 28. **Boxplot and the average volume of aggregates using STED microscopy in the Sph1-GFP aggregation model.** The boxplot represents the median and the range of values in each N (Left). The average and standard deviation volume of the aggregates was created in a bar plot (right).

According to both figures above (Figure 27 and Figure 28), there are not significant difference in values in the second and third N but can be used all Ns due to the similar median. Comparing the results of the average volume of Sph1-GFP aggregates (Table 3), both average and standard deviation looks different according to the type of microscopy used.

Table 3. **Values of average and standard deviation of Sph1-GFP aggregates.**

Type of Microscopy	Average Volume of Sph1-GFP aggregates
Confocal	32,36 ± 62,59 [µm³]
STED	6,44 ± 27,39 [µm³]

Having the difference in mind, the relation between the number of cells and volume with the number of aggregates per cell was created for both types of the microscopy in analysis. Meanwhile, the average and standard deviation value of the volume per N is also presented in Figure 29c and Figure 30c to represent the range of volume of aggregates that could occur in each N.

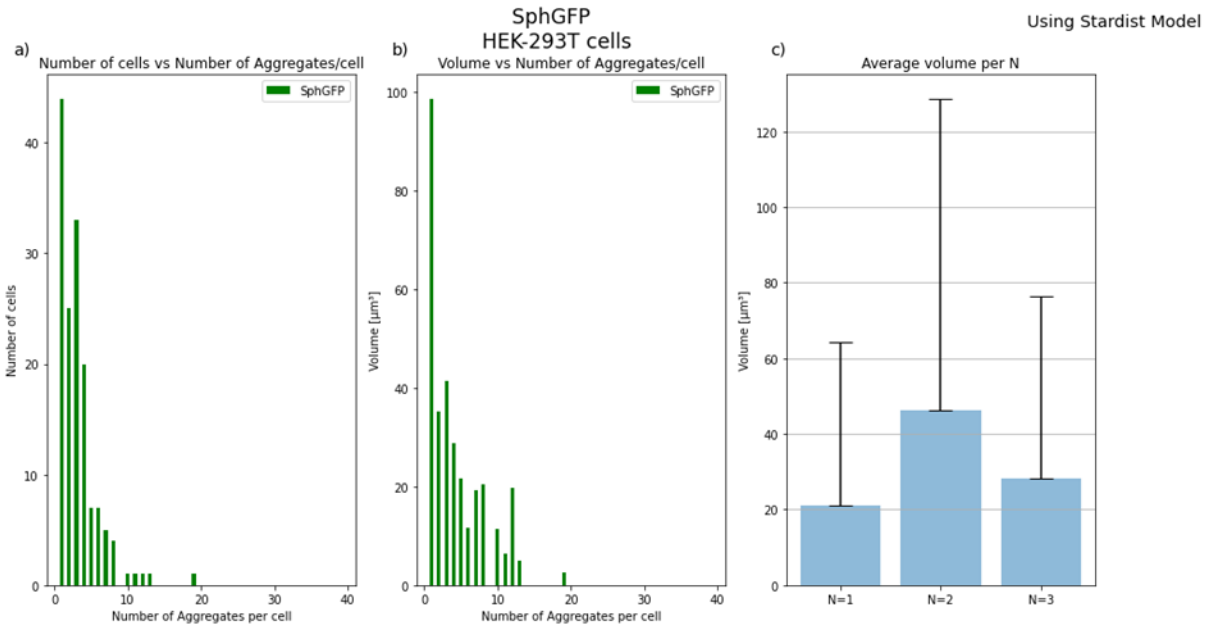

Figure 29. **Relation of number of cells and volume of aggregates with number of aggregates per cell. The average volume per N in confocal microscopy**. a) Bar plot of number of cells vs the number of aggregates in the Sph1-GFP aggregation model using confocal microscopy. b) Bar plot of average volume of the aggregates in each number of aggregates per cell in Sph1-GFP aggregation model using confocal microscopy. c) Bar plot with the average and standard deviation of the volume of aggregates per N.

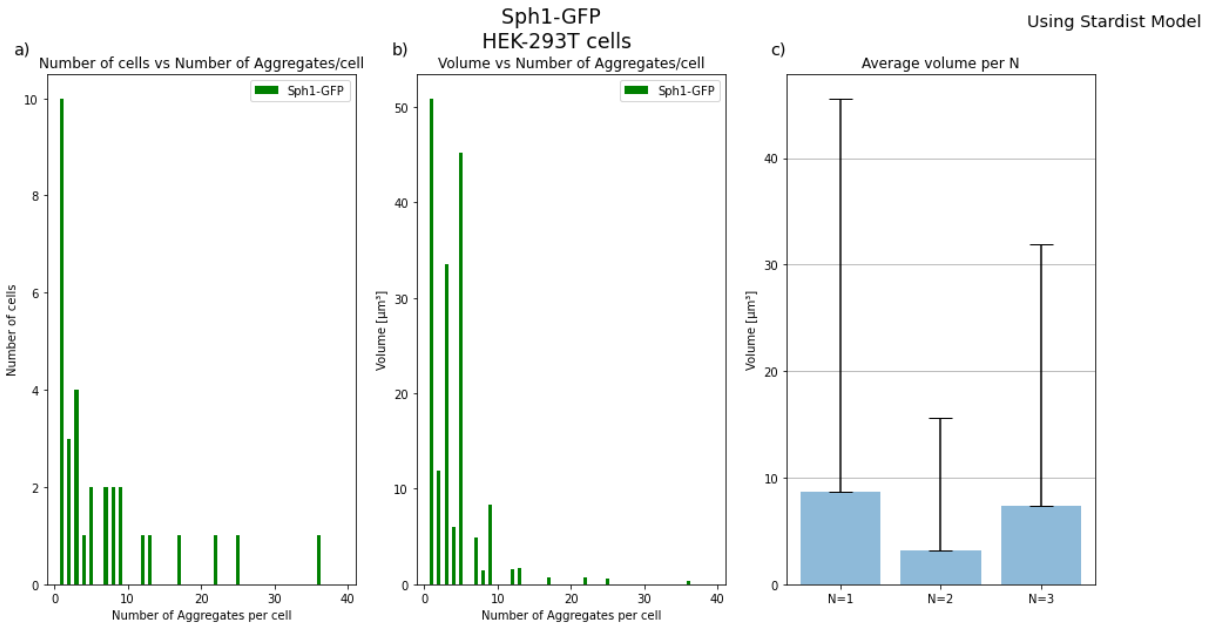

Figure 30. **Relation of number of cells and volume of aggregates with number of aggregates per cell. The average volume per N in STED microscopy.** a) Bar plot of number of cells vs the number of aggregates in the Sph1-GFP aggregation model using STED microscopy. b) Bar plot of average volume of the aggregates in each number of aggregates per cell in Sph1-GFP aggregation model using STED microscopy. c) Bar plot with the average and standard deviation of the volume of aggregates per N.

Therefore, the quantification of the previous graphs is presented in Table 4.

Table 4. **Values of average and standard deviation regarding the volume of aggregates, number of aggregates per cell and the average volume of aggregate per cell in Sph1-GFP aggregation model.**

Type of Microscopy	Average Volume of aggregates [µm³]	Average number of aggregates per cell [aggregates]	Average Volume of aggregates per cell [µm³]
Confocal	32,36 ± 62,59	3 ± 2	50,75 ± 55,77
STED	6,44 ± 27,39	8 ± 13	24,57 ± 37,60

For the SynTWT+Sph1 aggregation model, a box plot of the results of 50 images (one N) and the average and standard deviation of the aggregate volume per N and an average of the experiment were performed as well. Since one goal of the work is to consider the colocalization between the two signals of interest, a box plot of the average colocalization and max colocalization were performed. Then, an average and standard deviation for both variables were calculated. This process was the same in both microscopy types (Figure 31 and Figure 32 correspond to Confocal microscopy Figure 33 and Figure 34 correspond to STED microscopy).

To access the range of values achieved in terms of volume and colocalization in SynTWT+Sph1 aggregation model, a box plot for several variables was examined (Volume of the Aggregates in

SynTWT-Figure 31a and Figure 33a- and Sph1 channel- Figure 31c and Figure 33c) as well the average colocalization(Figure 31b and Figure 33b) and maximum colocalization (Figure 31d and Figure 33d).

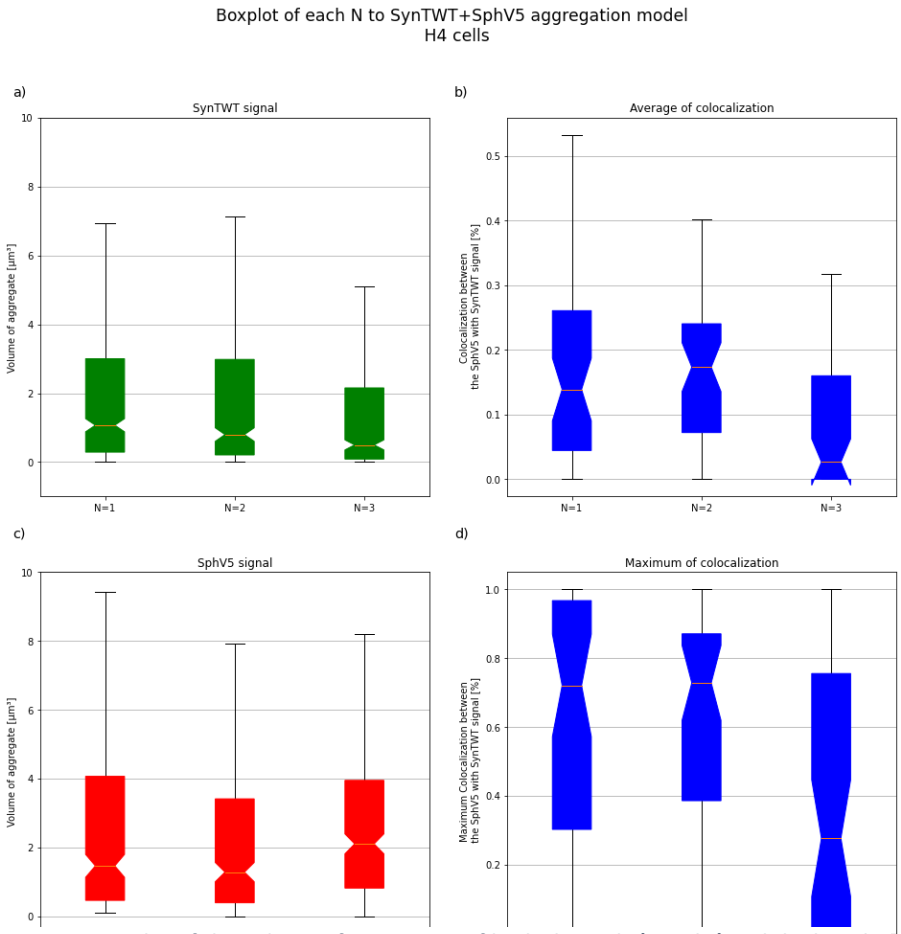

Figure 31. **Boxplot of the volume of aggregates of both channels (a and c) and the boxplot of average colocalization and maximum colocalization (b and d, respectively) using confocal microscopy in the SynTWT+SphV5 aggregation model.**

From SynTWT+Sph1 aggregation model and confocal microscopy, the difference from both volume of aggregate is not clear in confocal microscopy (Figure 31a and Figure 31c) although the difference in terms of median is around 1µm^3.

To evaluate the volume of aggregates in each channel and compare between them, in Figure *32*a a bar plot was created to compare in which the difference is smaller than 1µm^3. To evaluate the interaction, a bar plot was created to compare the average colocalization and the maximum colocalization in which the maximum colocalization has a big range of values while the average colocalization has a maximum around 0.3.

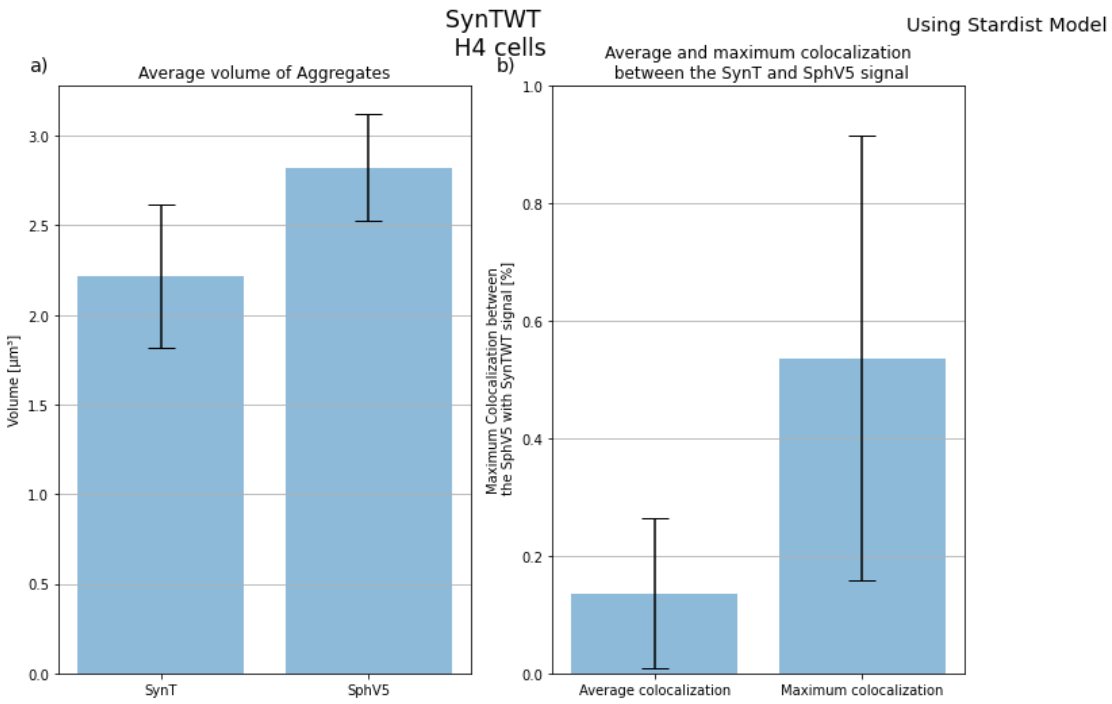

Figure 32. **Average volume of aggregates in both channels (a) and the average and standard deviation of variables average colocalization and maximum colocalization in SynTWT+Sph1 aggregation model using confocal microscopy (b).** The values are shown in Table 5 and Table 7 as well.

From the same aggregation model but from STED microscopy, the volume of the aggregates between the channel are slightly different (Figure *33*a and Figure *33*c). From STED microscopy, the evaluation of the colocalization was performed in the same way as confocal microscopy to evaluate in the same metric.

To access the hypothesis of interaction between the proteins, the average colocalization and maximum colocalization box plot was created (Figure *33*b and Figure *33*d).

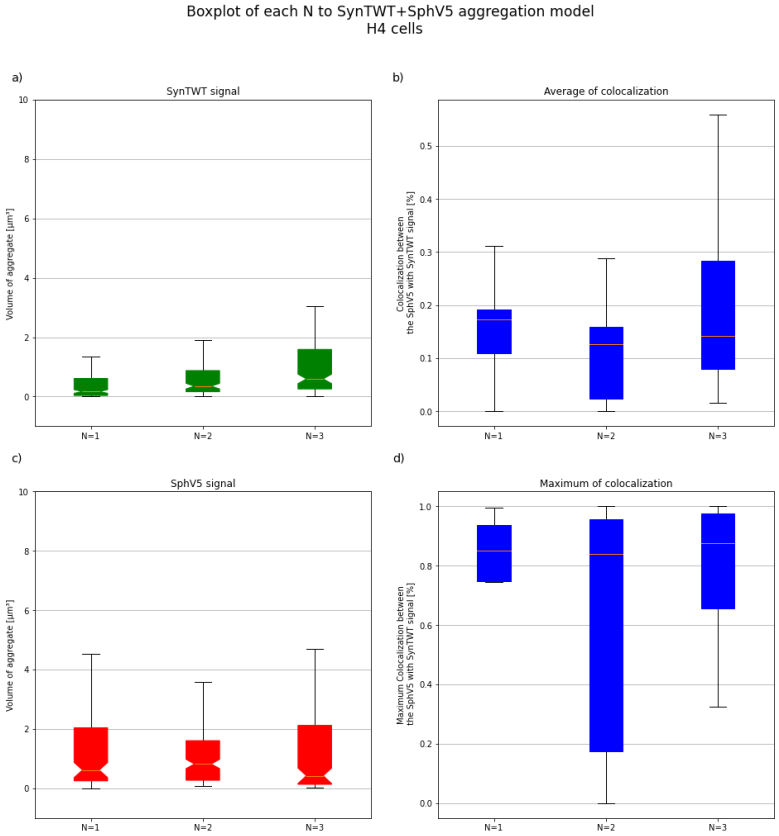

Figure 33. **Boxplot of the volume of aggregates of both channels (a and c) and the boxplot of average colocalization and maximum colocalization (b and d, respectively) using STED microscopy in the SynTWT+Sph1 aggregation model.**

To evaluate the volume of aggregates in each channel and compare between them, in Figure *34*a a bar plot was created to compare in which the difference is smaller than 1µm^3. To evaluate the interaction, a bar plot was created to compare the average colocalization and the maximum colocalization in which the maximum colocalization has a big range of values while the average colocalization has a maximum around 0.2 which is 0.1 lower than using the confocal microscopy.

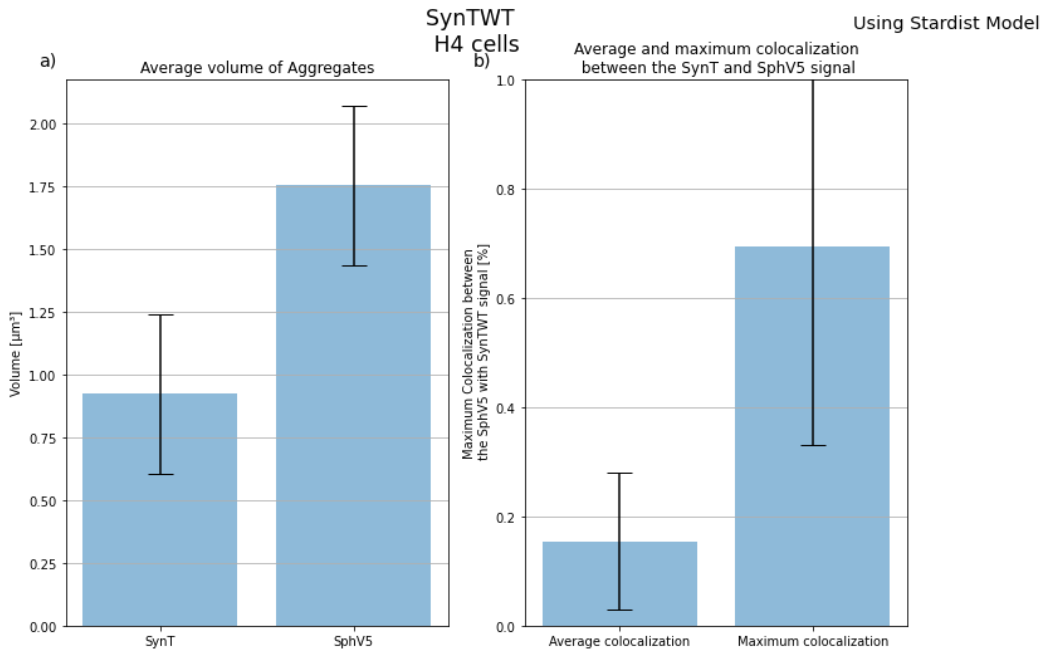

Figure 34. **Average volume of aggregates in both channels (a) and the average and standard deviation of variables average colocalization and maximum colocalization in SynTWT+Sph1 aggregation model using STED microscopy(b).** The values are shown in Table 5 and Table 7 as well.

To sum up the different results collected from the SynTWt+Sp1 aggregation model, the results of the average and standard deviation volume of SynT and Sph1 aggregates are shown in the Table 5. Both average and standard deviation look different according to the type of microscopy used.

Table 5. **Average and standard deviation of the SynTWT and Sph1 aggregates volume in both types of microscopies.**

Type of Microscopy	Average Volume of SynTWT aggregates [µm³]	Average Volume of Sph1 aggregates [µm³]
Confocal	2,37 ± 3,61	2,77 ± 4,21
STED	0,9 ± 1,70	1,70 ± 2,70

Having the difference between microscopies in mind, the relationship between the number of cells and volume with the number of aggregates per cell was created for both types of the microscopy in analysis to access the distribution of the aggregates according to the cells. Meanwhile, the average value of the volume per N is also presented in Figure 35 and Figure 36.

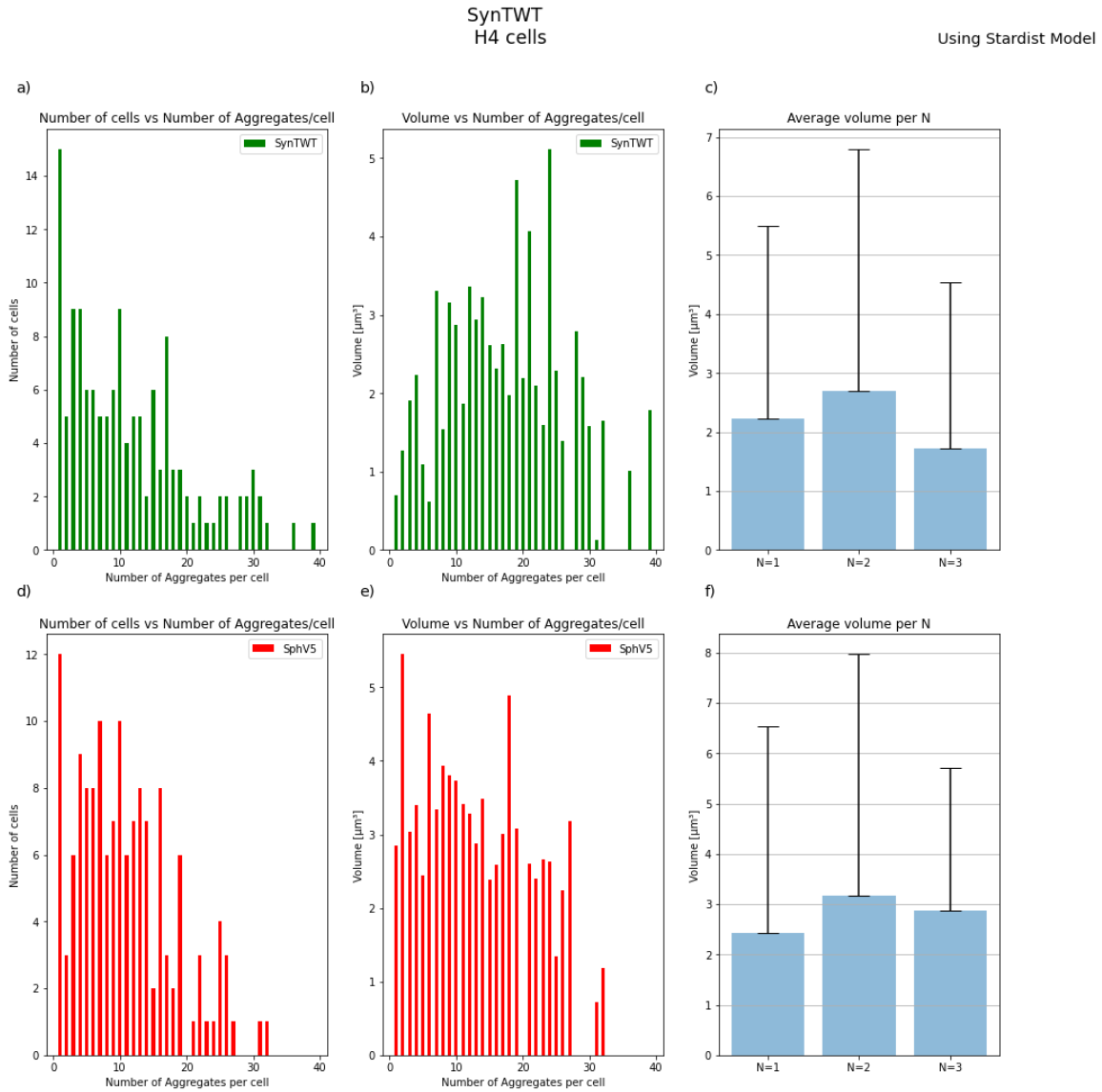

Figure 35. **Relation of number of cells and volume of aggregates with number of aggregates per cell. The average volume per N in confocal microscopy for each channel of interest (SynTWT-top and Sph1-bottom).** a) Bar plot of number of cells vs the number of aggregates regarding the SynTWT channel in the SynTWT+Sph1 aggregation model using confocal microscopy. b) Bar plot of average volume of the aggregates in each number of aggregates per cell regarding SynTWT channel in SynTWT+Sph1 aggregation model using confocal microscopy. c) Bar plot with the average and standard deviation of the volume of aggregates per N regarding the SynTWT channel. d) Bar plot of number of cells vs the number of aggregates regarding the Sph1 channel in the SynTWT+Sph1 aggregation model using confocal microscopy. e) Bar plot of average volume of the aggregates in each number of aggregates per cell regarding Sph1 channel in SynTWT+Sph1 aggregation model using confocal microscopy. f) Bar plot with the average and standard deviation of the volume of aggregates per N regarding the Sph1 channel.

In order to take the cell in account to evaluate the volume distribution of the aggregates in the cell, the relationship between the number of cells and the number of aggregates per cell was created that gives a range of number of aggregates per cell and the distribution of the number of aggregates across the experiments (Figure 35a,d and Figure 36a,d). With the evidence that the number of aggregates per cell vary, the evaluation of the influence in the volume was done recurring to a bar plot (Figure *35* b, e and Figure *36*b, d). Another metric was taken without the influence of the cell in

which a bar plot was created to conclude about the precision and the range of volume achieve in the aggregation process.

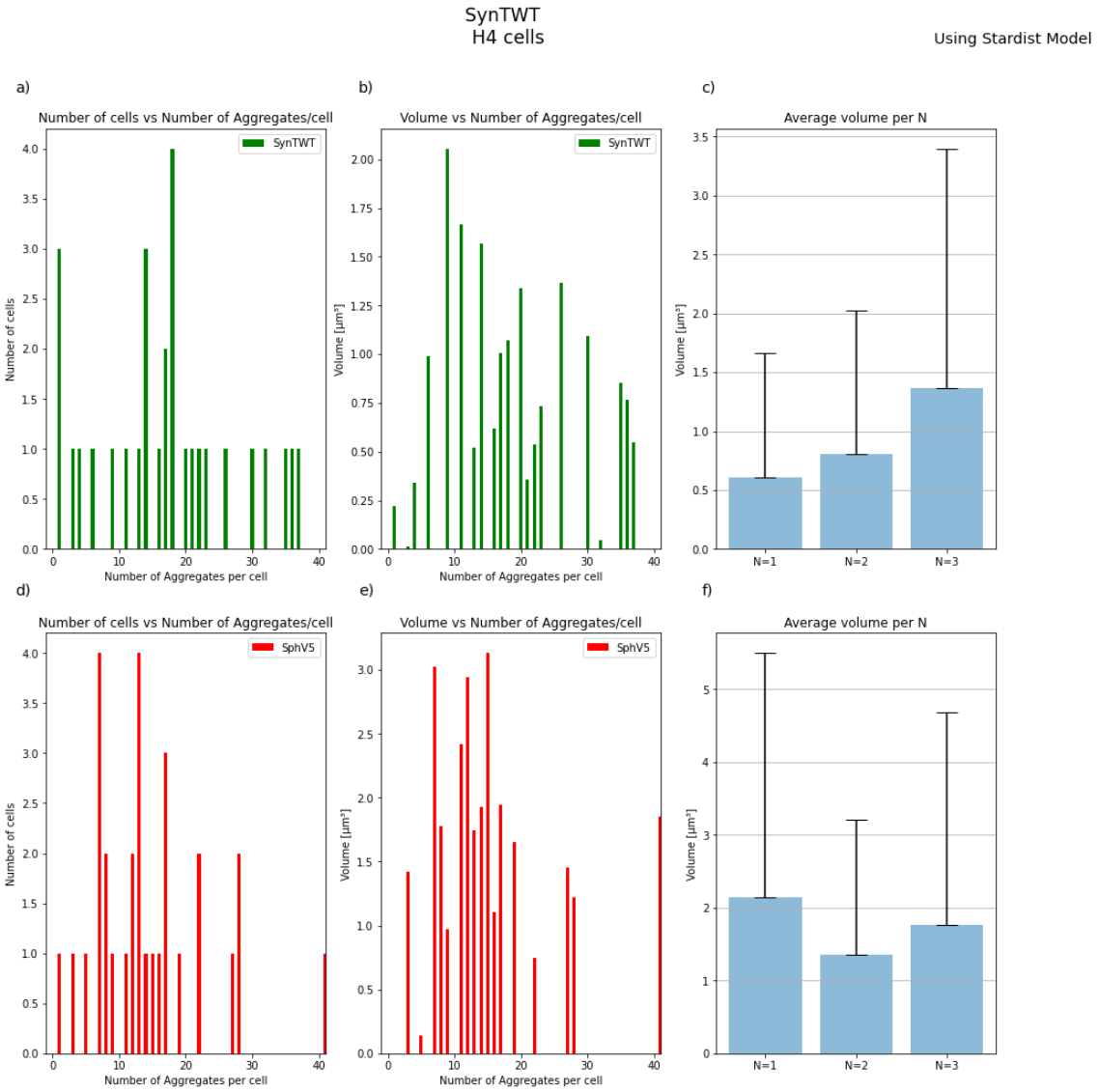

Figure 36. **Relationship between number of cells and volume of aggregates with number of aggregates per cell. The average volume per N in STED microscopy for each channel of interest (SynTWT-top and Sph1-bottom).** a) Bar plot of number of cells vs the number of aggregates regarding the SynTWT channel in the SynTWT+Sph1 aggregation model using STED microscopy. b) Bar plot of average volume of the aggregates in each number of aggregates per cell regarding SynTWT channel in SynTWT+Sph1 aggregation model using STED microscopy. c) Bar plot with the average and standard deviation of the volume of aggregates per N regarding the SynTWT channel. d) Bar plot of number of cells vs the number of aggregates regarding the Sph1 channel in the SynTWT+Sph1 aggregation model using STED microscopy. e) Bar plot of average volume of the aggregates in each number of aggregates per cell regarding Sph1 channel in SynTWT+Sph1 aggregation model using STED microscopy. f) Bar plot with the average and standard deviation of the volume of aggregates per N regarding the Sph1 channel.

Associating each type of microscopy (Figure 35 correspond to confocal microscopy and Figure 36 correspond to STED microscopy), the distribution in terms of the number of cells and volume of the aggregates regarding the number of aggregates was similar although the average volume is slightly different.

To sum up the values and quantifications, in Table 6 was displayed the average volume of aggregate, the average number of aggregates per cell and the average volume of aggregates per cells.

Table 6. **Values of average and standard deviation regarding the volume of aggregates, number of aggregates per cell and the average volume of aggregates per cell in SynTWT+Sph1 aggregation model.**

Type of Microscopy	Average Volume of Aggregate [µm ^{3}]	Average number of aggregates per cell [aggregates]	Average Volume of Aggregates per cell [µm3]
Confocal SynTWT	2,37 ± 3,61	14 ± 13	2,12 ± 1,83
STED SynTWT	0,9 ± 1,51	18 ± 11	0,88 ± 0,6
Confocal Sph1	2,77 ± 4,21	11 ± 10	3,17 ± 2,29
STED Sph1	1,70 ± 2,70	14 ± 8	1,81 ± 1,30

To access the colocalization between the proteins, it was calculated the mean of colocalization in each image and the maximum of colocalization in each image. Then, the average and standard deviation of each metric was calculated and presented in Table 7.

Table 7. **Average and standard deviation of mean colocalization and maximum colocalization between the Sph1 and SynTWT signal.**

Type of Microscopy	Mean of colocalization	Maximum Colocalization
Confocal	13,61 ± 12,71 %	53,61 ± 37,89 %
STED	15,46 ± 12,62 %	69.42 ± 36.35 %

Both variables look similar without significant difference which helps the hypothesis given in the 3D projections.

4. Discussion

The aggregation of αSyn is a central hallmark of several neurodegenerative diseases such as PD, however, the study of the biology and functions behind it remain poorly understood. Fluorescence microscopy has been a resourceful tool used in experiments in both cell and animal studies. Therefore, using fluorescence microscopy to analyse some of the aggregation model has been the major source of information.

Most of the images so far have been analysed in Maximum Intensity Projection which led to results and characterization of 2D images and carrying the problem of the localization in space. Thus, focusing on understanding how these aggregates are located in space is the next step in both the field of microscopy and biology. On one hand, the progress to find better techniques of analysis and setups to have a better resolution in all possible axes has been the major focus of microscopy. On the other hand, the accuracy of images and data help the biology to get a better understanding of some neurodegenerative diseases. Thus, both fields of study need to be in parallel and complement each other for best results leading to progress.

Analysing these images can use several protocols (Meijering et al., 2004; Puchkov, 2021; Rizk et al., 2014), the most important factor is the segmentation of the regions of interest. Deconvolution of the images and the creation of PSF to deconvolute can be the most accurate way to analyse (Rizk et al., 2014) although it is very bias to the interpretation of the user. Removing some noise using a given signal to noise ratio can improve the results as well. The protocol used in this study is very similar with (Rizk et al., 2014), although less features of the aggregate and less pre-processing of the image was done like the ones explained above. Therefore, this study can be used as a baseline to improve with more steps though the protocol to improve the accuracy of the protocols

One of the goals of the work was to create a volumed analysis of some aggregate models, this goal was achieved using a deep learning algorithm (Stardist (Schmidt et al., 2018; Weigert et al., 2020)) to segment in several aggregates and the relationship between those predicted slices. This method can be used in convex-shape polygon aggregates in order to get a volume of aggregate instead of area.

Another goal of the work was to compare different types of microscopy techniques to ensure what microscopy could be more suitable for the aggregation model in question. This goal was achieved using several techniques in different ranges of resolutions. Using Confocal Microscopy, a minimal resolution of 140,85nm in Sph1-GFP aggregation model was achieved (Elliott, 2020) and using STED microscopy, a minimal resolution of 75 nm in SynTWT aggregation model was achieved (van Dort, 2018; Wegner,

Ilgen, Gregor, Van Dort, et al., 2017). The hypothesis of finding the most suitable technique depending on the aggregation model in this study marks an important step to the way of analysing the spatial location of protein aggregation in the cell and the interaction of several proteins combining a more cost-efficient way of imaging the protein aggregation model. Therefore, comparing the results gathered and the time taken to record the data in both models, probably using STED in the Sph1-GFP aggregation model does not make it profitable to use due to the time spent in the technique. Although, the SynTWT+Sph1 aggregation model can be advantageous due to the number of aggregates and the size of them.

Sph1-GFP aggregation model

Sph1 has been studied in terms of formation of inclusions (Büttner et al., 2010; Tanaka et al., 2004), colocalization with several proteins (Chung et al., 2001) and its role in the PD (Krüger, 2004) although the analysis of the fluorescence images has been done by the number of aggregates or the area of those aggregates or even colocalization to other proteins by MIP or just a slice of the entire image. Therefore, the use of the real appearance of the protein can give better clues in the previous described topics.

According to the previous 3D projection of this aggregation model in confocal and STED microscopy, it seems that the size and shape are similar between them and round shape. Although when we statistically compare the results (Table *4*), the average result is one order below in STED than in confocal.

Analysing the relation to the number of cells in function of the number of aggregates per cell and the average volume in function of the number of aggregates per cell, some hypothesis can be raised. Comparing the number of cells in function of the number of aggregates per cell in each microscopy technique (Figure *29*a ,Figure *30*a), the shape of the graphs look similar but one difference needs to be taken in consideration. The low number of cells in STED microscopy probably can explain this difference in values. This reason can be transported to the average volume in function of the number of aggregates per cell where a small number of pictures taken can be a problem. When the number of aggregates is low, the average volume of those aggregates is big, achieving almost 100 μm^3 in confocal microscopy and 50 μm^3 in STED microscopy. To corroborate this hypothesis even more, the average volume of the aggregates per N in both microscopies are significantly different (Figure *29* and Figure *30*).

To understand the weight of each aggregate in the analysis and results, two different types of averaging were performed. (Volume of aggregates and volume of aggregates per cell). Between the

two variables, the difference is kept at the same level unless one difference can be taken. When all the aggregates have the same weight in the average, the result is lower which indicates that there are a lot of aggregates with a very small volume, but it is not dispersive through all cells. This might be due to the majority having large aggregates. The number of aggregates per cell corroborates the difference found between microscopy techniques, using STED, there are almost 3 times more aggregates per cell with a bigger range of values in contrast when compared in confocal microscopy (Figure *32* and Figure *34*).

This lack of similarity between these two types of microscopes can have several reasons. One reason can be the Z resolution. It used a 2D STED which then, some light can be transferred from different slices, this problem can happen in Confocal Microscopy, in other words, the PSF for each type of microscopy would be different. Another reason that can explain by the images used in the training. The model was trained with confocal microscopy images and one possibility of overcoming the issues would be to use images from STED to train the model. Another reason can be the difference of number of images, increasing the number of cells analysed in STED microscopy can be a solution or a way to test this hypothesis. Finally, using the 3D STED setup can be a solution as well in order to increase the resolution in the Z axis.

SynTWT+Sph1 aggregation model

Both proteins have been studied in several ways using several techniques in most of them analyse microscopy images in terms of areas (Nath et al., 2011) or number (Lázaro et al., 2014) reaching very small size and high number aggregates but reaching the values in terms of volume gives a more accurate result to the real aspect of the aggregate.

According to the previous 3D projection of this aggregation model in confocal and STED microscopy, it looks that the size and shape are similar in the essence with difference in the shape and space location. Although when we statistically compare the results (Table *5*), the average result is quite similar between the two.

In our study, we expected to have differences between the two types of microscopy techniques in terms of average aggregate volumes due to the small sizes, which could be facilitating the differentiation between the Confocal and STED microscopy in terms of principles but that did not happen.

Comparing first between the channels in Confocal Microscopy in terms of number of cells in function of number of aggregates per cell, the shape looks a little different. In other words, in SynTWT channel (green), most aggregates per cell are larger than Sph1 channel (Figure *35*). Most cells have below 20

aggregates per cell in both channels but more dispersed in the Sph1 channel. When comparing the Average Volume of Aggregate in function of number of aggregates per cell, the difference is quite clear in size of aggregate and shape of the graph.

In the SynTWT channel, the shape of the graph almost looks like a Gaussian distribution where the bigger aggregates can be found between 10 and 30 aggregates per cell. In contrast, the Sph1 channel, the shape of the graph looks more constant in function of the number of aggregates per cell. Therefore, we can assume that the volume of the aggregate is influenced by the number of aggregates in the cell in the SynTWT channel while it is not influenced in the Sph1 channel.

It is possible to discuss the size of the Aggregates in both channels, although the order of size is the same, the SynTWT aggregates are smaller than Sph1 aggregates. The standard deviation of SynTWT is also smaller than Sph1 aggregates which indicate the possibility of interaction between them as it has been published about αSyn inclusions in cultured cells (Liani et al., 2004; Luk et al., 2009).

Comparing the different values for volume of aggregates and volume of aggregates per cell between channels and types of microscopies can lead to several hypotheses. Considering the SynTWT and Sph1 marker images from Confocal Microscopy, the size of Sph1 aggregates is higher than SynTWT in both ways of calculating the average volume; that same relation is also applied in STED microscopy. The standard deviation of Sph1 aggregates is higher than SynTWT aggregates which can indicate a bigger range of values in terms of volume which can corroborate the idea of no interference of the number of aggregates per cell in contrast with the SynTWT aggregates (Luk et al., 2009).

In the same type of aggregates, using STED microscopy, the number of aggregates is higher and therefore, the use of 3D STED can be useful to create a better understanding of the spatial distribution of aggregates in all axes. Using this setup can take us to consider and probably reduce the PSF in the setup. This function could be evaluated in order to prove this hypothesis, because comparing both, we can conclude about the distinction between each slice of the image.

Although several proteins have been linked with aggregation of αSyn (Büttner et al., 2010; Casadei et al., 2014; Chung et al., 2001; Engelender et al., 1999; Liani et al., 2004; Lücking & Brice, 2000; Ribeiro et al., 2002; Swinnen et al., 2011), the hypothesis of interaction and therefore colocalization has been tested using several techniques (Luk et al., 2009). This study described that there is possible the interaction between them due to the fact of there are some colocalization. If we compare the results given by an object-based colocalization, the interaction does not seem very high. Checking several positions in the 3D projections of those proteins, it seems that interaction is different in terms of the Z axis. In other words, the Sph1 protein looks translated in Z compared with SynTWT protein. From previous studies in which the electron microscopy was used (Luk et al., 2009), the position of the

aggregates closer and starting closer to the nucleus have been described. That statement cannot be verified since the segmentation of the nucleus was not done. Using 3D STED could improve that differentiation in the axis to improve the capability of getting more accurate volumes of the aggregates.

These results can lead us to doubt about the real interaction between the aggregates and using different types of colocalization can be advantageous to classify that interaction.

Expansion Microscopy

Expansion Microscopy can lead us to several breakthroughs in terms of microscopy but still a lot to work on in terms of stability of the sample and viability of the protocols. The use of simple microscopes takes this technique to a very high ratio between results and feasibility.

The stability of the sample was the most difficult aspect to deal with. The expansion factor achieved during the experiments was 5.15 which is below present in (Truckenbrodt et al., 2018, 2019). Although, this technique can be used to overcome the diffraction limit, combining with confocal or STED can even more improve the resolution than it was achieved before (Truckenbrodt et al., 2018; Zwettler et al., 2020) . In Figure 18c, the background of the images is much larger than another type of microscopy presented in this work due to the use of a gel instead of glass slide with a more dispersive light in the gel. Therefore, this microscopy will need several steps before taking the same type of analysis. The filtering of the microscope will need to be very accurate because of the extensive time of exposure and the possibility of having signals in channels that we didn't desire. In order to remove some signal that can pass through to other channels, adaptative filters can be used (Peli & Lim, 1981).

To sum up, this study provided a method to evaluate the volume of the aggregates from two aggregate models associated with PD and the comparison between different microscopy in order to understand what the advantages are of using each technique. We also used some computational analysis which removed some biases that happen in the manual analysis by the researchers performing the studies. This could be used for a better time and cost efficiency in the future studies using the same models of aggregation and testing some possible therapeutic approaches.

5. Conclusions and future perspectives

Our work has provided a very simple but effective method to have a volume of protein aggregation in two models used in order to study the PD. The current work adds to our understanding and doubt the complex interaction between several proteins and the way to create the better technique for the model in question.

In summary, the current work has shown the importance of having analyses in 3 axes instead of two to create a better spatial resolution and localization of the aggregations of interest.

As future perspective, the results can be verified with more data from STED microscopy in order to create a better statistical analysis. Another work that can be done can be using the 3D segmentation instead of using 2D segmentation. The time to label the images will increase and the number of images for that will need to be higher as well. In contrast, the segmentation of the aggregates should be better, and the accuracy of the results will be higher to create an even more accurate spatial localization of each aggregate.

To validate the shape of the aggregates (shown in several 3D projections), the image of beads to prove the right PSF of the setup could be done. The shape of the beads will be known and therefore, the alignment according to the z axes could be measured more accurately.

The images used to train the models were from confocal microscopy. Changing these images to STED images or a model for each type of microscopy can be even better in order to create better results because each model is adapted to a specific type of microscopy. Labelling more images to add to the model can be a solution to create broader possibilities, especially in the SynT WT+Sph1 aggregation model in which the segmentation can be improved substantially.

6. References

Abeliovich, A., Schmitz, Y., Fariñas, I., Choi-Lundberg, D., Ho, W. H., Castillo, P. E., Shinsky, N., Garcia Verdugo, J. M., Armanini, M., Ryan, A., Hynes, M., Phillips, H., Sulzer, D., & Rosenthal, A. (2000). Mice lacking α-synuclein display functional deficits in the nigrostriatal dopamine system. *Neuron*, *25*(1), 239–252. https://doi.org/10.1016/S0896-6273(00)80886-7

Appel-Cresswell, S., Vilarino-Guell, C., Encarnacion, M., Sherman, H., Yu, I., Shah, B., Weir, D., Thompson, C., Szu-Tu, C., Trinh, J., Aasly, J. O., Rajput, A., Rajput, A. H., Jon Stoessl, A., & Farrer, M. J. (2013). Alpha-synuclein p.H50Q, a novel pathogenic mutation for Parkinson's disease. *Movement Disorders*, *28*(6), 811–813. https://doi.org/10.1002/MDS.25421

Biontex. (n.d.). *Transfection Methods*. Retrieved June 12, 2021, from https://www.biontex.com/en/transfection/

Blauwendraat, C., Heilbron, K., Vallerga, C. L., Bandres-Ciga, S., von Coelln, R., Pihlstrøm, L., Simón-Sánchez, J., Schulte, C., Sharma, M., Krohn, L., Siitonen, A., Iwaki, H., Leonard, H., Noyce, A. J., Tan, M., Gibbs, J. R., Hernandez, D. G., Scholz, S. W., Jankovic, J., … Singleton, A. B. (2019). Parkinson's disease age at onset genome-wide association study: Defining heritability, genetic loci, and α-synuclein mechanisms. *Movement Disorders*, *34*(6), 866–875. https://doi.org/10.1002/mds.27659

Bonin, M., Marx, F. P., Kautzmann, S., Riess, O., & Krüger, R. (2008). Microarray expression analysis reveals genetic pathways implicated in C621 synphilin-1-mediated toxicity. *Journal of Neural Transmission*, *115*(7), 941–958. https://doi.org/10.1007/s00702-008-0031-x

Bossy-Wetzel, E., Schwarzenbacher, R., & Lipton, S. A. (2004). Molecular pathways to neurodegeneration. *Nature Medicine*, *10*(7), S2–S9. https://doi.org/10.1038/nm1067

Bousset, L., Pieri, L., Ruiz-Arlandis, G., Gath, J., Jensen, P. H., Habenstein, B., Madiona, K., Olieric, V., Böckmann, A., Meier, B. H., & Melki, R. (2013). ARTICLE Structural and functional characterization of two alpha-synuclein strains. *Nature Communications*. https://doi.org/10.1038/ncomms3575

Burré, J., Sharma, M., Tsetsenis, T., Buchman, V., Etherton, M., & Südhof, T. C. (2010). *α-Synuclein Promotes SNARE-Complex Assembly in vivo and in vitro* (Vol. 329, Issue

5999).

Büttner, S., Delay, C., Franssens, V., Bammens, T., Ruli, D., Zaunschirm, S., de Oliveira, R. M., Outeiro, T. F., Madeo, F., Buée, L., Galas, M. C., & Winderickx, J. (2010). Synphilin-1 enhances a-synuclein aggregation in yeast and contributes to cellular stress and cell death in a sir2-dependent manner. *PLoS ONE*, *5*(10). https://doi.org/10.1371/journal.pone.0013700

Caicedo, J. C., Roth, J., Goodman, A., Becker, T., Karhohs, K. W., Broisin, M., Molnar, C., Mcquin, C., Singh, S., Theis, F. J., Carpenter, A. E., & Library, O. (2019). *Evaluation of Deep Learning Strategies for Nucleus Segmentation in Fluorescence Images in Wiley*. https://doi.org/10.1002/cyto.a.23863

Casadei, N., Pö Hler, A.-M., Tomá S-Zapico, C., Torres-Peraza, J. S., Schwedhelm, I., Witz, A., Zamolo, I., De Heer, R., Spruijt, B., Noldus, L. P. J. J., Klucken, J., Lucas, J. J., Kahle, P. J., Krü Ger, R., Riess, O., & Nuber, S. (2014). Overexpression of synphilin-1 promotes clearance of soluble and misfolded alpha-synuclein without restoring the motor phenotype in aged A30P transgenic mice. *Human Molecular Genetics*, *23*(3), 767–781. https://doi.org/10.1093/hmg/ddt467

Chartier-Harlin, M. C., Kachergus, J., Roumier, C., Mouroux, V., Douay, X., Lincoln, S., Levecque, C., Larvor, L., Andrieux, J., Hulihan, M., Waucquier, N., Defebvre, L., Amouyel, P., Farrer, M., & Destée, A. (2004). α-synuclein locus duplication as a cause of familial Parkinson's disease. *The Lancet*, *364*(9440), 1167–1169. https://doi.org/10.1016/S0140-6736(04)17103-1

Chozinski, T. J., Halpern, A. R., Okawa, H., Kim, H., Tremel, G. J., Wong, R. O. L., & Vaughan, J. C. (2016). Expansion microscopy with conventional antibodies and fluorescent proteins. *Nature Methods*, *April*, 1–7. https://doi.org/10.1038/nmeth.3833

Chung, K. K. K., Zhang, Y., Lim, K. L., Tanaka, Y., Huang, H., Gao, J., Ross, C. A., Dawson, V. L., & Dawson, T. M. (2001). Parkin ubiquitinates the α-synuclein–interacting protein, synphilin-1: implications for Lewy-body formation in Parkinson disease. *Nature Medicine*, *7*(10), 1144–1150. https://doi.org/10.1038/nm1001-1144

Conway, K. A., Rochet, J. C., Ding, T. T., Harper, J. D., Williamson, R. E., & Lansbury, P. T. (2000). Accelerated Oligomerization by Parkinson's Disease Linked α-Synuclein Mutants. *Annals of the New York Academy of Sciences*, *920*(1), 42–45. https://doi.org/10.1111/J.1749-6632.2000.TB06903.X

Cuervo, A. M., Stafanis, L., Fredenburg, R., Lansbury, P. T., & Sulzer, D. (2004). Impaired degradation of mutant α-synuclein by chaperone-mediated autophagy. *Science*, *305*(5688), 1292–1295. https://doi.org/10.1126/SCIENCE.1101738/SUPPL_FILE/CUERVO.SOM.PDF

D'Este, E., Kamin, D., Göttfert, F., El-Hady, A., & Hell, S. W. (2015). STED Nanoscopy Reveals the Ubiquity of Subcortical Cytoskeleton Periodicity in Living Neurons. *Cell Reports*, *10*(8), 1246–1251. https://doi.org/https://doi.org/10.1016/j.celrep.2015.02.007

Danzer, K. M., & Mclean, P. J. (2011). *Drug Targets from Genetics: Alpha-Synuclein*.

Davidovits, P., & Egger, M. D. (1971). Scanning Laser Microscope for Biological Investigations. *Appl. Opt.*, *10*(7), 1615–1619. https://doi.org/10.1364/AO.10.001615

DAVIDOVITS, P. M. D. E. (1969). *Scanning Laser Microscope* (p. 831). Nature.

de Chaumont, F., Dallongeville, S., Chenouard, N., Hervé, N., Pop, S., Provoost, T., Meas-Yedid, V., Pankajakshan, P., Lecomte, T., Le Montagner, Y., Lagache, T., Dufour, A., & Olivo-Marin, J.-C. (2012). Icy: an open bioimage informatics platform for extended reproducible research. *Nature Methods*, *9*(7), 690–696. https://doi.org/10.1038/nmeth.2075

Dima, A. A., Elliott, J. T., Filliben, J. J., Halter, M., Peskin, A., Bernal, J., Kociolek, M., Brady, M. C., Tang, H. C., & Plant, A. L. (2011). Comparison of Segmentation Algorithms For Fluorescence Microscopy Images of Cells. *Original Article Cytometry Part A*, *79*, 545–559. https://doi.org/10.1002/cyto.a.21079

Elliott, A. D. (2020). Confocal Microscopy: Principles and Modern Practices. *Current Protocols in Cytometry*, *92*(1). https://doi.org/10.1002/cpcy.68

Engelender, S., Kaminsky, Z., Xin, G., Sharp, A. H., Amaravi, R. K., Kleiderlein, J. J., Margolis, R. L., Troncoso, J. C., Lanahan, A. A., Worley, P. F., Dawson, V. L., Dawson, T. M., & Ross, C. A. (1999). Synphilin-1 associates with α-synuclein and promotes the formation of cytosolic inclusions. *Nature Genetics 1999 22:1*, *22*(1), 110–114. https://doi.org/10.1038/8820

Fares, M. B., Ait-Bouziad, N., Dikiy, I., Mbefo, M. K., Jovičić, A., Kiely, A., Holton, J. L., Lee, S. J., Gitler, A. D., Eliezer, D., & Lashuel, H. A. (2014). The novel Parkinson's disease linked mutation G51D attenuates in vitro aggregation and membrane binding of α-synuclein, and enhances its secretion and nuclear localization in cells. *Human*

Molecular Genetics, *23*(17), 4491–4509. https://doi.org/10.1093/hmg/ddu165

Genet, N. (2014). Large-scale meta-analysis of genome-wide association data identifies six new risk loci for Parkinson's disease HHS Public Access Author manuscript. *Nat Genet*, *46*(9), 989–993. https://doi.org/10.1038/ng.3043

Gitler, A. D., Dhillon, P., & Shorter, J. (2017). Neurodegenerative disease: Models, mechanisms, and a new hope. *DMM Disease Models and Mechanisms*, *10*(5), 499–502. https://doi.org/10.1242/DMM.030205

Goedert, M. (2001). Alpha-synuclein and neurodegenerative diseases. *Nature Reviews Neuroscience*, *2*(7), 492–501. https://doi.org/10.1038/35081564

Gonçalves, S., & Outeiro, T. F. (2013). Assessing the subcellular dynamics of alpha-synuclein using photoactivation microscopy. *Molecular Neurobiology*, *47*(3), 1081–1092. https://doi.org/10.1007/s12035-013-8406-x

Greten-Harrison, B., Polydoro, M., Morimoto-Tomita, M., Diao, L., Williams, A. M., Nie, E. H., Makani, S., Tian, N., Castillo, P. E., Buchman, V. L., & Chandra, S. S. (2010). αβγ-Synuclein triple knockout mice revealage-dependent neuronal dysfunction. *Proceedings of the National Academy of Sciences of the United States of America*, *107*(45), 19573–19578. https://doi.org/10.1073/pnas.1005005107

Grys, B. T., Lo, D. S., Sahin, N., Kraus, O. Z., Morris, Q., Boone, C., & Andrews, B. J. (2017). Machine learning and computer vision approaches for phenotypic profiling. *Journal of Cell Biology*, *216*(1), 65–71. https://doi.org/10.1083/JCB.201610026

Harke, B., Keller, J., Ullal, C. K., Westphal, V., Schönle, A., & Hell, S. W. (2008). Resolution scaling in STED microscopy. *Optics Express*, *16*(6), 4154. https://doi.org/10.1364/oe.16.004154

Hartl, F. U., & Hayer-Hartl, M. (2009). Converging concepts of protein folding in vitro and in vivo. *Nature Structural & Molecular Biology*, *16*(6), 574–581. https://doi.org/10.1038/nsmb.1591

Hell, S. W., & Wichmann, J. (1994). Breaking the diffraction resolution limit by stimulated emission: stimulated-emission-depletion fluorescence microscopy. *Opt. Lett.*, *19*(11), 780–782. https://doi.org/10.1364/OL.19.000780

Huang, Y., Cheung, L., Rowe, D., & Halliday, G. (2004). Genetic contributions to Parkinson's

disease. *Brain Research Reviews*, *46*(1), 44–70. https://doi.org/10.1016/J.BRAINRESREV.2004.04.007

Kan, A. (2017). Machine learning applications in cell image analysis. *Immunology and Cell Biology*, *95*, 525–530. https://doi.org/10.1038/icb.2017.16

Kass, M., Witkin, A., & Terzopoulos, D. (1988). Snakes: Active contour models. *International Journal of Computer Vision*, *1*(4), 321–331. https://doi.org/10.1007/BF00133570

Kawamata, H., Mclean, P. J., Sharma, N., & Hyman, B. T. (2001). International Society for Neurochemistry. In *929±934 Journal of Neurochemistry* (Vol. 77).

Koprich, J. B., Kalia, L. V, & Brotchie, J. M. (2017). Animal models of α-synucleinopathy for Parkinson disease drug development. *Nature Publishing Group*, *18*. https://doi.org/10.1038/nrn.2017.75

Krüger, R. (2004). The role of synphilin-1 in synaptic function and protein degradation. In *Cell and Tissue Research* (Vol. 318, Issue 1, pp. 195–199). https://doi.org/10.1007/s00441-004-0953-z

Krüger, R., Kuhn, W., Müller, T., Woitalla, D., Graeber, M., Kösel, S., Przuntek, H., Epplen, J. T., Schöls, L., & Riess, O. (1998). AlaSOPro mutation in the gene encoding α-synuclein in Parkinson's disease. *Nature Genetics 1998 18:2*, *18*(2), 106–108. https://doi.org/10.1038/ng0298-106

Lázaro, D. F., Rodrigues, E. F., Langohr, R., Shahpasandzadeh, H., Ribeiro, T., Guerreiro, P., Gerhardt, E., Kröhnert, K., Klucken, J., Pereira, M. D., Popova, B., Kruse, N., Mollenhauer, B., Rizzoli, S. O., Braus, G. H., Danzer, K. M., & Outeiro, T. F. (2014). Systematic Comparison of the Effects of Alpha-synuclein Mutations on Its Oligomerization and Aggregation. *PLoS Genetics*, *10*(11). https://doi.org/10.1371/journal.pgen.1004741

Lesage, S., Anheim, M., Letournel, F., Bousset, L., Honoré, A., Rozas, N., Pieri, L., Madiona, K., Dürr, A., Melki, R., Verny, C., & Brice, A. (2013). G51D α-synuclein mutation causes a novel Parkinsonian–pyramidal syndrome. *Annals of Neurology*, *73*(4), 459–471. https://doi.org/10.1002/ANA.23894

Li, J., Uversky, V. N., & Fink, A. L. (2001). Effect of Familial Parkinson's Disease Point Mutations A30P and A53T on the Structural Properties, Aggregation, and Fibrillation of Human α-Synuclein†. *Biochemistry*, *40*(38), 11604–11613.

https://doi.org/10.1021/BI010616G

Liani, E., Eyal, A., Avraham, E., Shemer, R., Szargel, R., Berg, D., Bornemann, A., Riess, O., Ross, C. A., Rott, R., & Engelender, S. (2004). Ubiquitylation of synphilin-1 and α-synuclein by SIAH and its presence in cellular inclusions and Lewy bodies imply a role in Parkinson's disease. *Proceedings of the National Academy of Sciences of the United States of America*, *101*(15), 5500–5505. https://doi.org/10.1073/pnas.0401081101

Lipson, S. G., Lipson, H., & Tannhauser, D. S. (1995). *Optical Physics*. Cambridge University Press. https://doi.org/10.1017/CBO9781139170413

Lücking, C. B., & Brice, A. (2000). Alpha-synuclein and Parkinson's disease. *Cellular and Molecular Life Sciences CMLS 2000 57:13*, *57*(13), 1894–1908. https://doi.org/10.1007/PL00000671

Luk, K. C., Song, C., O'Brien, P., Stieber, A., Branch, J. R., Brunden, K. R., Trojanowski, J. Q., & Lee, V. M. Y. (2009). Exogenous α-synuclein fibrils seed the formation of Lewy body-like intracellular inclusions in cultured cells. *Proceedings of the National Academy of Sciences of the United States of America*, *106*(47), 20051–20056. https://doi.org/10.1073/pnas.0908005106

Maroteaux, L., & Scheller, R. H. (1991). The rat brain synucleins; family of proteins transiently associated with neuronal membrane. *Molecular Brain Research*, *11*(3–4), 335–343. https://doi.org/10.1016/0169-328X(91)90043-W

Marvian, A. T., Koss, D. J., Aliakbari, F., Morshedi, D., & Outeiro, T. F. (2019). In vitro models of synucleinopathies: informing on molecular mechanisms and protective strategies. *Journal of Neurochemistry*, *150*(5), 535–565. https://doi.org/10.1111/jnc.14707

Matsumoto, B. (2002). *Cell Biological Applications of Confocal Microscopy*. Elsevier Science. https://books.google.de/books?id=k8ZpAAAAMAAJ

McLean, P. J., Kawamata, H., Ribich, S., & Hyman, B. T. (2000). Membrane Association and Protein Conformation of α-Synuclein in Intact Neurons: EFFECT OF PARKINSON′S DISEASE-LINKED MUTATIONS *. *Journal of Biological Chemistry*, *275*(12), 8812–8816. https://doi.org/10.1074/JBC.275.12.8812

McQuin, C., Goodman, A., Chernyshev, V., Kamentsky, L., Cimini, B. A., Karhohs, K. W., Doan, M., Ding, L., Rafelski, S. M., Thirstrup, D., Wiegraebe, W., Singh, S., Becker, T.,

Caicedo, J. C., & Carpenter, A. E. (2018). *CellProfiler 3.0: Next-generation image processing for biology*. https://doi.org/10.1371/journal.pbio.2005970

Nath, S., Goodwin, J., Engelborghs, Y., & Pountney, D. L. (2011). Raised calcium promotes α-synuclein aggregate formation. *Molecular and Cellular Neuroscience*, *46*(2), 516–526. https://doi.org/10.1016/J.MCN.2010.12.004

Otsu, N. (1979). A Threshold Selection Method from Gray-Lavel Histograms. *EEE TRANSACTIONS ON SYSTREMS*, *9*(12), 62–66. https://doi.org/10.1128/AAC.03728-14

Outeiro, T. F., & Mestre, T. A. (2019). Synuclein Meeting 2019: where we are and where we need to go. *Journal of Neurochemistry*, *150*(5), 462–466. https://doi.org/10.1111/jnc.14825

Parkinson, J. (2002). An essay on the shaking palsy. 1817. *The Journal of Neuropsychiatry and Clinical Neurosciences*, *14*(2). https://doi.org/10.1176/jnp.14.2.223

Pasanen, P., Myllykangas, L., Siitonen, M., Raunio, A., Kaakkola, S., Lyytinen, J., Tienari, P. J., Pöyhönen, M., & Paetau, A. (2014). A novel α-synuclein mutation A53E associated with atypical multiple system atrophy and Parkinson's disease-type pathology. *Neurobiology of Aging*, *35*(9), 2180.e1-2180.e5. https://doi.org/10.1016/J.NEUROBIOLAGING.2014.03.024

Patrick Weish, Diana F. Lázaro, Luís Palmares, Patrícia I. Santos, Christine Stadelmann, Günter U. Höglinger, Silvio O. Rizzoli, T. F. O. (n.d.). *Super-resolution microscopy informs on the molecular architecture of alpha-synuclein inclusions in model systems and in the human brain*.

Pawley, J. (2006). *Confocal Handbook.Pdf* (p. 4).

Peli, T., & Lim, J. (1981). Adaptive filtering for image enhancement. *ICASSP '81. IEEE International Conference on Acoustics, Speech, and Signal Processing*, *6*, 1117–1120. https://doi.org/10.1109/ICASSP.1981.1171130

Perkins, W. A. (1980). Area Segmentation of Images Using Edge Points. *IEEE Transactions on Pattern Analysis and Machine Intelligence*, *PAMI-2*(1), 8–15. https://doi.org/10.1109/TPAMI.1980.4766965

Polymeropoulos, M. H., Lavedan, C., Leroy, E., Ide, S. E., Dehejia, A., Dutra, A., Pike, B., Root, H., Rubenstein, J., Boyer, R., Stenroos, E. S., Chandrasekharappa, S.,

Athanassiadou, A., Papapetropoulos, T., Johnson, W. G., Lazzarini, A. M., Duvoisin, R. C., Di Iorio, G., Golbe, L. I., & Nussbaum, R. L. (1997). Mutation in the α-Synuclein Gene Indentified in Families with Parkinson's Disease. *Science*, *276*(5321), 2045–2047. http://www.jstor.org/stable/2892982

Preim, B., & Bartz, D. (2007). *Visualization in Medicine: Theory, Algorithms, and Applications*. Morgan Kaufmann Publishers Inc.

Proukakis, C., Dudzik, C. G., Brier, T., MacKay, D. S., Cooper, J. M., Millhauser, G. L., Houlden, H., & Schapira, A. H. (2013). A novel α-synuclein missense mutation in Parkinson disease. *Neurology*, *80*(11), 1062. https://doi.org/10.1212/WNL.0B013E31828727BA

Ribeiro, C. S., Carneiro, K., Ross, C. A., Menezes, J. R. L., & Engelender, S. (2002). Synphilin-1 is developmentally localized to synaptic terminals, and its association with synaptic vesicles is modulated by α-synuclein. *Journal of Biological Chemistry*, *277*(26), 23927–23933. https://doi.org/10.1074/JBC.M201115200

Ronneberger, O., Fischer, P., & Brox, T. (2015). *LNCS 9351 - U-Net: Convolutional Networks for Biomedical Image Segmentation*. https://doi.org/10.1007/978-3-319-24574-4_28

Schindelin, J., Arganda-Carreras, I., Frise, E., Kaynig, V., Longair, M., Pietzsch, T., Preibisch, S., Rueden, C., Saalfeld, S., Schmid, B., Tinevez, J.-Y., White, D. J., Hartenstein, V., Eliceiri, K., Tomancak, P., & Cardona, A. (2012). Fiji: an open-source platform for biological-image analysis. *Nature Methods*, *9*(7), 676–682. https://doi.org/10.1038/nmeth.2019

Schmidt, U., Weigert, M., Broaddus, C., & Myers, G. (2018). Cell detection with star-convex polygons. *Lecture Notes in Computer Science (Including Subseries Lecture Notes in Artificial Intelligence and Lecture Notes in Bioinformatics)*, *11071 LNCS*, 265–273. https://doi.org/10.1007/978-3-030-00934-2_30

Schulz-Schaeffer, W. J. (2015). Is Cell Death Primary or Secondary in the Pathophysiology of Idiopathic Parkinson's Disease? *Biomolecules*, *5*(3), 1467–1479. https://doi.org/10.3390/BIOM5031467

Shirakashi, Y., Kawamoto, Y., Tomimoto, H., Takahashi, R., & Ihara, M. (2006). α-Synuclein is colocalized with 14-3-3 and synphilin-1 in A53T transgenic mice. *Acta Neuropathologica*, *112*(6), 681–689. https://doi.org/10.1007/S00401-006-0132-2

Singleton, A. B., Farrer, M., Johnson, J., Singleton, A., Hague, S., Kachergus, J., Hulihan, M., Peuralinna, T., Dutra, A., Nussbaum, R., Lincoln, S., Crawley, A., Hanson, M., Maraganore, D., Adler, C., Cookson, M. R., Muenter, M., Baptista, M., Miller, D., … Gwinn-Hardy, K. (2003). α-Synuclein Locus Triplication Causes Parkinson's Disease. *Science*, *302*(5646), 841. https://doi.org/10.1126/SCIENCE.1090278/SUPPL_FILE/SINGLETON.SOM.PDF

Swinnen, E., Büttner, S., Outeiro, T. F., Galas, M. C., Madeo, F., Winderickx, J., & Franssens, V. (2011). Aggresome formation and segregation of inclusions influence toxicity of α-synuclein and synphilin-1 in yeast. *Biochemical Society Transactions*, *39*(5), 1476–1481. https://doi.org/10.1042/BST0391476

Tanaka, M., Kim, Y. M., Lee, G., Junn, E., Iwatsubo, T., & Mouradian, M. M. (2004). Aggresomes Formed by α-Synuclein and Synphilin-1 Are Cytoprotective. *Journal of Biological Chemistry*, *279*(6), 4625–4631. https://doi.org/10.1074/JBC.M310994200

Taylor, J. P., Hardy, J., & Fischbeck, K. H. (2002). Toxic Proteins in Neurodegenerative Disease. *Science*, *296*(5575), 1991–1995. https://doi.org/10.1126/SCIENCE.1067122

Truckenbrodt, S., Maidorn, M., Crzan, D., Wildhagen, H., Kabatas, S., & Rizzoli, S. O. (2018). X10 expansion microscopy enables 25-nm resolution on conventional microscopes. *EMBO Reports*, *19*(9). https://doi.org/10.15252/embr.201845836

Truckenbrodt, S., Sommer, C., Rizzoli, S. O., & Danzl, J. G. (2019). A practical guide to optimization in X10 expansion microscopy. *Nature Protocols*, *14*(3), 832–863. https://doi.org/10.1038/s41596-018-0117-3

V5 Tab Properties. (n.d.). https://www.ptglab.com/news/blog/v5-tag-properties/

Valente, E. M., Arena, G., Torosantucci, L., & Gelmetti, V. (2012). Molecular pathways in sporadic PD. *Parkinsonism & Related Disorders*, *18*(SUPPL. 1), S71–S73. https://doi.org/10.1016/S1353-8020(11)70023-2

van Dort, J. (2018). *Aberration correction in STED microscopy*. *October*, 1–74. https://ediss.uni-goettingen.de/bitstream/handle/21.11130/00-1735-0000-0005-12B4-B/Dissertation_JorisvanDort.pdf?sequence=1

Varghese, A., Tenbroek, E. M., Coles, J. J., & Sigg, D. C. (2006). Endogenous channels in HEK cells and potential roles in HCN ionic current measurements. *Progress in Biophysics and Molecular Biology*, *90*(1–3), 26–37.

https://doi.org/10.1016/j.pbiomolbio.2005.05.002

Vidyadhara, D. J., Lee, J. E., & Chandra, S. S. (2019). Role of the endolysosomal system in Parkinson's disease. *Journal of Neurochemistry*, *150*(5), 487–506. https://doi.org/10.1111/jnc.14820

Vincent, L., & Soille, P. (1991). Watersheds in digital spaces: an efficient algorithm based on immersion simulations. *IEEE Transactions on Pattern Analysis and Machine Intelligence*, *13*(6), 583–598. https://doi.org/10.1109/34.87344

Wakabayashi, K., Engelender, S., Tanaka, Y., Yoshimoto, M., Mori, F., Tsuji, S., Ross, C. A., & Takahashi, H. (2001). Immunocytochemical localization of synphilin-1, an α-synuclein-associated protein, in neurodegenerative disorders. *Acta Neuropathologica 2001 103:3*, *103*(3), 209–214. https://doi.org/10.1007/S004010100451

Weber, M., Leutenegger, M., Stoldt, S., Jakobs, S., Mihaila, T. S., Butkevich, A. N., & Hell, S. W. (2021). MINSTED fluorescence localization and nanoscopy. *Nature Photonics*, *15*(May). https://doi.org/10.1038/s41566-021-00774-2

Wegner, W., Ilgen, P., Gregor, C., van Dort, J., Mott, A. C., Steffens, H., & Willig, K. I. (2017). In vivo mouse and live cell STED microscopy of neuronal actin plasticity using far-red emitting fluorescent proteins. *Scientific Reports*, *7*(1), 11781. https://doi.org/10.1038/s41598-017-11827-4

Wegner, W., Ilgen, P., Gregor, C., Van Dort, J., Mott, A. C., Steffens, H., & Willig, K. I. (2017). In vivo mouse and live cell STED microscopy of neuronal actin plasticity using far-red emitting fluorescent proteins. *Scientific Reports*, *7*(1). https://doi.org/10.1038/s41598-017-11827-4

Weigert, M., Schmidt, U., Haase, R., Sugawara, K., & Myers, G. (2020). Star-convex polyhedra for 3D object detection and segmentation in microscopy. *Proceedings - 2020 IEEE Winter Conference on Applications of Computer Vision, WACV 2020*, 3655–3662. https://doi.org/10.1109/WACV45572.2020.9093435

Wiesmann, V., Franz, D., Held, C., Münzenmayer, C., Palmisano, R., & Wittenberg, T. (2015). Review of free software tools for image analysis of fluorescence cell micrographs. *Journal of Microscopy*, *257*(1), 39–53. https://doi.org/10.1111/JMI.12184

Willig, K. I., Steffens, H., Gregor, C., Herholt, A., Rossner, M. J., & Hell, S. W. (2014). Nanoscopy of filamentous actin in cortical dendrites of a living mouse. *Biophysical*

Journal, *106*(1). https://doi.org/10.1016/J.BPJ.2013.11.1119

Xie, Y.-Y., Zhou, C.-J., Zhou, Z.-R., Hong, J., Che, M.-X., Fu, Q.-S., Song, A.-X., Lin, D.-H., & Hu, H.-Y. (2010). Interaction with synphilin-1 promotes inclusion formation of α-synuclein: mechanistic insights and pathological implication. *The FASEB Journal*, *24*(1), 196–205. https://doi.org/10.1096/fj.09-133082

Zarranz, J. J., Alegre, J., Gómez-Esteban, J. C., Lezcano, E., Ros, R., Ampuero, I., Vidal, L., Hoenicka, J., Rodriguez, O., Atarés, B., Llorens, V., Gomez Tortosa, E., Del Ser, T., Muñoz, D. G., & De Yebenes, J. G. (2004). The new mutation, E46K, of α-synuclein causes parkinson and Lewy body dementia. *Annals of Neurology*, *55*(2), 164–173. https://doi.org/10.1002/ANA.10795

Zhang, J., & Hu, J. (2008). Image Segmentation Based on 2D Otsu Method with Histogram Analysis. *2008 International Conference on Computer Science and Software Engineering*, *6*, 105–108. https://doi.org/10.1109/CSSE.2008.206

Zwettler, F. U., Reinhard, S., Gambarotto, D., Bell, T. D. M., Hamel, V., Guichard, P., & Sauer, M. (2020). Molecular resolution imaging by post-labeling expansion single-molecule localization microscopy (Ex-SMLM). *Nature Communications*, *11*(1). https://doi.org/10.1038/s41467-020-17086-8